Study of a Coulomb Centre in Graphene under Magnetic Field

towards tuning the super-critical atomic collapse

Student: Wang Sihao (A0070858W)
Supervisor: Vitor Manuel Pereira

Department of Physics
National University of Singapore
Singapore
April 7, 2014

Abstract

This thesis has reviewed the properties of graphene and the occurrence of super-critical atomic collapse. It has also shown the result of a weak Coulomb impurity in a magnetic field to establish the limiting case. In this case, our calculation approach was validated almost in real time with the appearance of the experimental paper [13]. The bending of the Landau levels in the vicinity of the charged impurity observed in those experiments is entirely captured by our perturbative treatment and our prediction for the dependence of the LDOS on energy and distance to the impurity. Various methods have been employed to attack the problem under a strong magnetic field, but no satisfactory solutions have obtained thus far. Ideas of using a semi-classical approach or a numerical study are discussed at the end of the thesis.

Contents

Chapter 1

Introduction

Since its first isolation in 2004 [1], graphene has gained popularity quickly. Thanks to its peculiar properties such as the linear energy dispersion, there is an intense interest in understanding graphene and much progress was made over the years. Furthermore, the unusual behavior of electrons in graphene opened the door to the study of many other areas. In particular, the existence of Dirac fermions in graphene has rendered the traditional quantum electrodynamics problem of supercritical atomic collapse tractable in a laboratory setting. Theoretical studies of supercritical atomic collapse in graphene have been published by several groups [2, 3]. However, it was not until recently that an experimental evidence of supercritical atomic collapse was observed in graphene [4]. This experimental proof of existence of supercritical atomic collapse in graphene has naturally led to the investigation of the same phenomenon in a magnetic field. This is the main theme of this final year thesis.

There are several works on the effect of a magnetic field on electrons in graphene [5, 6]. However, the focus was only on the sub-critical region. The nature of the super-critical region remains elusive and requires attention. In view of the current situation, it is important and meaningful to investigate the nature of the super-critical region so as to enhance the understanding of graphene and atomic collapse.

This thesis is organized as follows. Chapter 2 will briefly discuss the derivation of the 2D Dirac equation and the electronic response to a Coulomb impurity in both sub- and super-critical regions. Chapter 3 will establish the case of the effect of a weak impurity to Landau Levels in graphene, which could then be used as a reference to the case of a strong

impurity in the supercritical region. Chapter 4 will attempt to address the problem of the electronic response to both strong electric and magnetic fields and investigate the nature of the supercritical atomic collapse under a strong magnetic field.

Chapter 2

The Coulomb Impurity in Graphene

2.1 The Dirac Hamiltonian of Electrons in Graphene

Graphene is essentially a single-layered carbon sheet. The carbon atoms are arranged in a honeycomb structure as shown in Fig. 2.1.

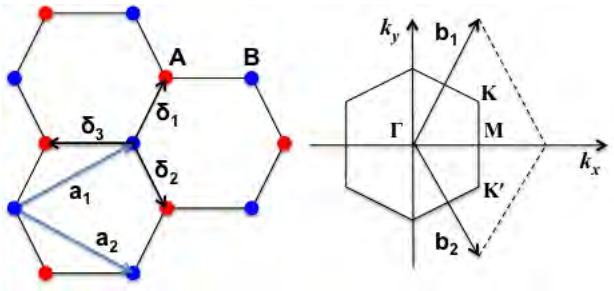

Figure 2.1: Left: the honeycomb lattice structure of graphene. The two sub-lattices are denoted by different colors (red and blue). Right: the corresponding Brillouin zone. The Dirac cones are located at the **K** and **K**′ points.

This honeycomb structure is made up of two identical sub-lattices. The lattice vectors in real space as shown in Fig. 2.1 can be expressed as

$$\mathbf{a}_1 = \frac{a}{2}\begin{pmatrix} 3 \\ \sqrt{3} \end{pmatrix}, \qquad \mathbf{a}_2 = \frac{a}{2}\begin{pmatrix} 3 \\ -\sqrt{3} \end{pmatrix}, \tag{2.1}$$

where $a = 1.42$Å, is the distance to the nearest neighbor. The corresponding reciprocal

lattice vectors are also shown in Fig. 2.1

$$\mathbf{b}_1 = \frac{2\pi}{3a}\begin{pmatrix} 1 \\ \sqrt{3} \end{pmatrix}, \qquad \mathbf{b}_2 = \frac{2\pi}{3a}\begin{pmatrix} 1 \\ -\sqrt{3} \end{pmatrix}. \tag{2.2}$$

Two points in the Brillouin zone of graphene are of significant importance, which are called the Dirac points, for the reason that will be explained later,

$$\mathbf{K} = \begin{pmatrix} 2\pi/3a \\ 2\pi/3\sqrt{3}a \end{pmatrix}, \qquad \mathbf{K}' = \begin{pmatrix} 2\pi/3a \\ -2\pi/3\sqrt{3}a \end{pmatrix}. \tag{2.3}$$

The three nearest-neighbor vectors in real space are

$$\boldsymbol{\delta}_1 = \frac{a}{2}\begin{pmatrix} 1 \\ \sqrt{3} \end{pmatrix}, \quad \boldsymbol{\delta}_2 = \frac{a}{2}\begin{pmatrix} 1 \\ -\sqrt{3} \end{pmatrix}, \quad \boldsymbol{\delta}_1 = -a\begin{pmatrix} 1 \\ 0 \end{pmatrix}. \tag{2.4}$$

In the tight-binding model, electrons are assumed to hop only to both the nearest and the second-nearest atoms. In this chapter, the unit system is used such that $\hbar = 1$. The effective Hamiltonian is

$$\hat{H} = -t_1 \sum_{i,j,\sigma} \left(\hat{a}^\dagger_{i,\sigma} \hat{b}_{j,\sigma} + \hat{b}^\dagger_{j,\sigma} \hat{a}_{i,\sigma} \right) - t_2 \sum_{i,j,\sigma} \left(\hat{a}^\dagger_{i,\sigma} \hat{a}_{j,\sigma} + \hat{a}^\dagger_{j,\sigma} \hat{a}_{i,\sigma} + \hat{b}^\dagger_{i,\sigma} \hat{b}_{j,\sigma} + \hat{b}^\dagger_{j,\sigma} \hat{b}_{i,\sigma} \right), \tag{2.5}$$

where $\hat{a}_{\sigma,i}$ $\left(\hat{a}^\dagger_{\sigma,i}\right)$ is the annihilation (creation) operator of an electron with a spin $\sigma = \pm\frac{1}{2}$ on site $\mathbf{R}_i$ on the sub-lattice A. The corresponding operators for sub-lattice B are $\hat{b}_{\sigma,i}$ $\left(\hat{b}^\dagger_{\sigma,i}\right)$. $t_1 \approx 2.8eV$ is the nearest-neighbor hopping energy and t_2 is the second-nearest-neighbor hopping energy.

The energy spectrum (Fig. 2.2) of this Hamiltonian is well-known [7], and has the form

$$E_\pm(\mathbf{k}) = \pm t_1 \sqrt{3 + f(\mathbf{k})} - t_2 f(\mathbf{k}), \tag{2.6}$$

with

$$f(\mathbf{k}) = 2\cos(\sqrt{3}k_y a) + 4\cos(\frac{\sqrt{3}}{2}k_y a)\cos(\frac{3}{2}k_x a). \tag{2.7}$$

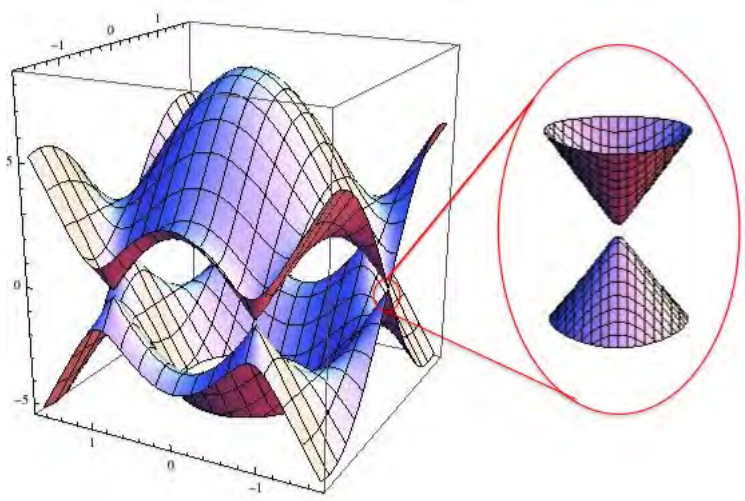

Figure 2.2: Left: the energy spectrum of graphene, with $t_1 = 2.7$ eV and $t_2 = -0.2t_1$. Right: a zoom-in view of the energy band near one of the Dirac points.

Here E_+ refers to the upper band and E_- to the lower band. We expand Eq. 2.6 in the vicinity of $\mathbf{K}$ or $\mathbf{K}'$ point in terms of $\mathbf{k} = \mathbf{K} + \mathbf{q}$, where $|\mathbf{q}| \ll |\mathbf{K}|$ is the momentum vector from the Dirac point. The result gives

$$E_\pm(\mathbf{q}) \approx \pm v_F |\mathbf{q}|, \tag{2.8}$$

where $v_F = 3t_1 a/2 \approx 1 \times 10^6$ m/s is the Fermi velocity. First derived in [7], this result shows remarkable difference from the usual low energy dispersion relation in conventional metals and semiconductors $E(\mathbf{q}) = q^2/2m$. The Fermi velocity v_F in graphene does not depend on energy or momentum, unlike the usual velocity $v = k/m = \sqrt{2E/m}$, which does have a momentum or energy dependence. Furthermore, the dispersion relationship is linear in graphene, unlike the quadratic dependence in the normal case. Thus this is termed "the linear dispersion relationship". As shown in Fig. 2.2, this linear dispersion relationship has a conic shape and thus is termed as "the Dirac cone".

The reason for naming $\mathbf{K}$ and $\mathbf{K}'$ points as "Dirac points" and the linear dispersion relationship as "Dirac cone" is that electrons in graphene obey the 2D Dirac equation. To derive this 2D Dirac equation, we take Eq. 2.5 with $t_2 = 0$ and use the Fourier transform

of the electron operators [8],

$$a_n = \frac{1}{\sqrt{N_c}} \sum_{\mathbf{k}} e^{-i\mathbf{k}\cdot\mathbf{R}_n} a(\mathbf{k}), \tag{2.9}$$

where N_c is the number of unit cells. Under this transformation, we can express a_n from two terms, which come from the Fourier sum around $\mathbf{K}$ and $\mathbf{K}'$ points. This gives approximately

$$a_n \approx e^{-i\mathbf{K}\cdot\mathbf{R}_n} a_{\mathbf{K},n} + e^{-i\mathbf{K}'\cdot\mathbf{R}_n} a_{\mathbf{K}',n}, \tag{2.10}$$

$$b_n \approx e^{-i\mathbf{K}\cdot\mathbf{R}_n} b_{\mathbf{K},n} + e^{-i\mathbf{K}'\cdot\mathbf{R}_n} b_{\mathbf{K}',n}. \tag{2.11}$$

These new operators, $a_{\mathbf{K}(\mathbf{K}'),n}$ and $b_{\mathbf{K}(\mathbf{K}'),n}$, are assumed to vary slowly over the unit cell. Expanding these operators up to a linear order in $\boldsymbol{\delta}$, we obtain [9],

$$\hat{H} = -iv_F \int dxdy \left[\hat{\Psi}_1^\dagger(\mathbf{r})\boldsymbol{\sigma}\cdot\boldsymbol{\nabla}\hat{\Psi}_1(\mathbf{r}) + \hat{\Psi}_2^\dagger(\mathbf{r})\boldsymbol{\sigma}^*\cdot\boldsymbol{\nabla}\hat{\Psi}_2(\mathbf{r})\right], \tag{2.12}$$

where $\boldsymbol{\sigma} = (\sigma_x, \sigma_y)$, $\boldsymbol{\sigma}^* = (\sigma_x, -\sigma_y)$, $\hat{\Psi}_i = (a_i, b_i)$, and $\hat{\Psi}_i^\dagger = (a_i^\dagger, b_i^\dagger)$. It is clear that this Hamiltonian has two massless Dirac-like contributions, one for $\mathbf{K}$ and the other for $\mathbf{K}'$. Thus in the first quantized language, the 2D Dirac equation governing the two-component electron wave function $\psi(\mathbf{r})$, close to the $\mathbf{K}$ point, is

$$-iv_F\boldsymbol{\sigma}\cdot\boldsymbol{\nabla}\Psi(\mathbf{r}) = \epsilon\Psi(\mathbf{r}), \tag{2.13}$$

or the effective Hamiltonian for the valley $\mathbf{K}$ reads

$$\hat{H}_{\mathbf{K}} = v_F\boldsymbol{\sigma}\cdot\hat{\mathbf{p}}. \tag{2.14}$$

The corresponding Hamiltonian for $\mathbf{K}'$ is

$$\hat{H}_{\mathbf{K}'} = v_F\boldsymbol{\sigma}^*\cdot\hat{\mathbf{p}}. \tag{2.15}$$

In general, for a system with non-zero effective mass, the effective-mass Hamiltonian is

$$\hat{H} = v_F \left(\sigma_1 \hat{p}_x + \lambda \sigma_2 \hat{p}_y\right) + \sigma_3 M v_F^2, \tag{2.16}$$

where v_F is the Fermi velocity of the electrons, $\hat{p}_{x,y}$ are the 2D momentum operator, σ_i are the Pauli matrices, $\lambda = \pm 1$ are for $\mathbf{K}$ and $\mathbf{K}'$ points, and M is the effective mass of electrons.

2.2 Wave Functions of Free Electrons in Graphene

With reference mainly to [2, 10], this section aims to derive the 2D electron wave function. In subsequent calculations, the effective-mass Hamiltonian is given by Eq. 2.16, and v_F is set to unity. The idea is to solve the following eigen-problem with $\lambda = +1$ and $\Psi(\mathbf{r}) = \begin{pmatrix} \phi \\ \chi \end{pmatrix} = \begin{pmatrix} \alpha \\ \beta \end{pmatrix} e^{i\mathbf{p}\cdot\mathbf{r}}$

$$\hat{H}\Psi(\mathbf{r}) = \epsilon \Psi(\mathbf{r}), \tag{2.17}$$

which in the matrix form is

$$\begin{pmatrix} M & p_x - ip_y \\ p_x + ip_y & -M \end{pmatrix} \begin{pmatrix} \phi \\ \chi \end{pmatrix} = \epsilon \begin{pmatrix} \phi \\ \chi \end{pmatrix}. \tag{2.18}$$

It is straightforward to get $p_x^2 + p_y^2 = \epsilon^2 - M^2$ or $\epsilon = \pm\sqrt{p^2 + M^2}$ where $p^2 = p_x^2 + p_y^2$. On the other hand, since

$$\begin{pmatrix} M & p_x - ip_y \\ p_x + ip_y & -M \end{pmatrix} \begin{pmatrix} \alpha \\ \beta \end{pmatrix} e^{i\mathbf{p}\cdot\mathbf{r}} = \epsilon \begin{pmatrix} \alpha \\ \beta \end{pmatrix} e^{i\mathbf{p}\cdot\mathbf{r}}, \tag{2.19}$$

the coupled equations in terms of α and β are

$$(ip_x + p_y)\,\beta = (\epsilon - M)\alpha, \tag{2.20}$$

$$(-ip_x + p_y)\,\beta^* = (\epsilon - M)\alpha^*. \tag{2.21}$$

Normalization is set in such a way that there is one particle in a unit volume $\Psi^\dagger\Psi = 1$. This means that $\alpha^*\alpha + \beta^*\beta = 1$. With this condition, the solutions for electrons ($\epsilon > M$) to Eq. 2.20 and Eq. 2.21 are

$$\alpha = \frac{1}{\sqrt{2\epsilon}}\sqrt{|\epsilon + M|}, \tag{2.22}$$

$$\beta = \frac{1}{\sqrt{2\epsilon}}\sqrt{|\epsilon - M|}. \tag{2.23}$$

The corresponding solution for holes ($\epsilon < -M$) is $\beta = -\frac{1}{\sqrt{2|\epsilon|}}\sqrt{|\epsilon - M|}$. In general, α and β differ by a relative phase $e^{i\delta}$, the two-component wave function is thus

$$\Psi(\mathbf{r}) = \begin{pmatrix} \phi \\ \chi \end{pmatrix} = \frac{1}{\sqrt{2|\epsilon|}} \begin{pmatrix} \sqrt{|\epsilon + M|} \\ \pm e^{i\delta}\sqrt{|\epsilon - M|} \end{pmatrix}, \tag{2.24}$$

with $\pm$ for electrons and holes respectively.

For the ease of calculation involving a Coulomb impurity which has rotation symmetry later, it is helpful to express the effective Hamiltonian in cylindrical coordinates,

$$\begin{pmatrix} M & e^{-i\theta}\left(-i\partial_r - \frac{1}{r}\partial_\theta\right) \\ e^{i\theta}\left(-i\partial_r + \frac{1}{r}\partial_\theta\right) & -M \end{pmatrix} \begin{pmatrix} \phi \\ \chi \end{pmatrix} = \epsilon \begin{pmatrix} \phi \\ \chi \end{pmatrix}. \tag{2.25}$$

The coupled equations for χ and ϕ are

$$e^{-i\theta}(-i\partial_r - \frac{1}{r}\partial_\theta)\chi = (\epsilon - M)\phi, \tag{2.26}$$

$$e^{i\theta}(-i\partial_r + \frac{1}{r}\partial_\theta)\phi = (\epsilon + M)\chi, \tag{2.27}$$

which can be decoupled as

$$-\frac{1}{r}\frac{\partial}{\partial r}\left(r\frac{\partial}{\partial r}\chi\right) - \frac{1}{r^2}\left(\frac{\partial^2\chi}{\partial\theta^2} - i\frac{\partial\chi}{\partial\theta}\right) = p^2\chi, \tag{2.28}$$

$$-\frac{1}{r}\frac{\partial}{\partial r}\left(r\frac{\partial}{\partial r}\phi\right) - \frac{1}{r^2}\left(\frac{\partial^2\phi}{\partial\theta^2} + i\frac{\partial\phi}{\partial\theta}\right) = p^2\phi. \tag{2.29}$$

Eq. 2.28 and Eq. 2.29 show that the components of the spinor wave function are separable in terms of radial and angular components. This implies that the spinor could be expressed

as

$$\begin{pmatrix} \phi(\mathbf{r}) \\ \chi(\mathbf{r}) \end{pmatrix} = \begin{pmatrix} F(r)e^{im\theta} \\ iG(r)e^{in\theta} \end{pmatrix}, \tag{2.30}$$

where $F(r)$ and $G(r)$ are the radial functions and $e^{im(n)\theta}$ accounts for the angular contribution. The imaginary number i is introduced to simplify the subsequent calculations.

Substitution of Eq. 2.30 in Eq. 2.18 gives

$$e^{i(n-1)\theta}\left(-i\frac{\partial}{\partial r} - \frac{in}{r}\right)(iG(r)) = (\epsilon - M)F(r)e^{im\theta}. \tag{2.31}$$

The radial and angular parts must equal each other on both sides of the equation. This means

$$e^{i(n-1)\theta} = e^{im\theta}, \tag{2.32}$$

or

$$m = n - 1. \tag{2.33}$$

With this constraint of $m = n - 1$, Eq. 2.18 gives

$$\frac{dG}{dr} + \frac{m+1}{r}G = (\epsilon - M)F, \tag{2.34}$$

$$-\frac{dF}{dr} + \frac{m}{r}G = (\epsilon + M)G, \tag{2.35}$$

which could be further separated

$$-\frac{d^2F}{dr^2} - \frac{1}{r}\frac{dF}{dr} + \frac{m^2}{r^2}F = p^2F, \tag{2.36}$$

$$-\frac{d^2G}{dr^2} - \frac{1}{r}\frac{dG}{dr} + \frac{(m+1)^2}{r^2}G = p^2G. \tag{2.37}$$

Eq. 2.36 and Eq. 2.37 have the same form as the radial solution to the non-relativistic

Schrödinger equation of hydrogen, so the solutions are of in the form

$$F(r) = AR_m(r) = A\sqrt{2\pi p}J_m(pr) \sim A\frac{2}{\sqrt{r}}\cos\left(pr - \frac{m\pi}{2} - \frac{\pi}{4}\right), \tag{2.38}$$

$$G(r) = BR_{m+1}(r) = B\sqrt{2\pi p}J_{m+1}(pr) \sim B\frac{2}{\sqrt{r}}\cos\left(pr - \frac{m\pi}{2} - \frac{3\pi}{4}\right). \tag{2.39}$$

To determine the coefficients A and B, consider Eq. 2.30, which gives that

$$\frac{\chi}{\phi} = \frac{iGe^{in\theta}}{Fe^{im\theta}} = \frac{iBJ_m(pr)}{AJ_{m+1}(pr)} = \pm\sqrt{\left|\frac{\epsilon - M}{\epsilon + M}\right|}e^{i\theta}. \tag{2.40}$$

With the relation that $J_m(\infty)/J_{m+1}(\infty) = 1$ and $\theta = 0$, Eq. 2.40 becomes

$$\frac{iB}{A} = \pm\sqrt{\left|\frac{\epsilon - M}{\epsilon + M}\right|}. \tag{2.41}$$

This finally gives the expression of the spinor

$$\Psi(\mathbf{r}) = \frac{1}{\sqrt{2|\epsilon|}}\begin{pmatrix} \sqrt{|\epsilon + M|}R_m(r)e^{im\theta} \\ \pm i\sqrt{|\epsilon - M|}R_{m+1}(r)e^{i(m+1)\theta} \end{pmatrix}. \tag{2.42}$$

It is worth noting that the projection of total angular momentum along the z axis

$$\hat{j}_z = \hat{l}_z + \frac{1}{2}\hat{\sigma}, \tag{2.43}$$

where $\hat{l}_z = -i\partial_\theta$ is the angular momentum in the z direction and $\frac{1}{2}\hat{\sigma}_z$ is the isospin, commutes with $\hat{H}$, since

$$\left[\hat{l}_z, \hat{H}\right] = i(\sigma_x\hat{p}_y - \sigma_y\hat{p}_x) \ ; \qquad \left[\frac{1}{2}\hat{\sigma}_z, \hat{H}\right] = -i(\sigma_x\hat{p}_y - \sigma_y\hat{p}_x). \tag{2.44}$$

Thus the wave function in Eq. 2.42 is also an eigenstate of $\hat{j}_z$ with the eigenvalue $j = m + 1/2$. Eq. 2.42 can thus be rewritten as

$$\Psi(\mathbf{r}) = \frac{1}{\sqrt{2|\epsilon|}}\begin{pmatrix} \sqrt{|\epsilon + M|}R_{j-1/2}(r)e^{i\left(j-\frac{1}{2}\right)\theta} \\ \pm i\sqrt{|\epsilon - M|}R_{j+1/2}(r)e^{i\left(j+\frac{1}{2}\right)\theta} \end{pmatrix}. \tag{2.45}$$

In graphene, the effective mass of electrons is zero, Eq. 2.45 is then reduced to

$$\Psi(\mathbf{r}) = \frac{1}{\sqrt{2}} \begin{pmatrix} R_{j-1/2} e^{i\left(j-\frac{1}{2}\right)\theta} \\ \pm i R_{j+1/2} e^{i\left(j+\frac{1}{2}\right)\theta} \end{pmatrix}. \tag{2.46}$$

This is the 2D wave function of free electrons in graphene.

2.3 Coulomb Impurity in Graphene

The effective Hamiltonian of graphene with an attractive Coulomb impurity is given by

$$\hat{H} = v_F \left(\boldsymbol{\sigma} \cdot \hat{\mathbf{p}} - \frac{g}{r} \right), \tag{2.47}$$

where $g = Ze^2/(4\pi\epsilon_0 v_F)$.

Taking the plus solution, Eq. 2.46 can be rewritten as

$$\Psi(\mathbf{r}) = \frac{1}{\sqrt{r}} \begin{pmatrix} \phi_A e^{i\left(j-\frac{1}{2}\right)\theta} \\ i\phi_B e^{i\left(j+\frac{1}{2}\right)\theta} \end{pmatrix}, \tag{2.48}$$

where pre-fracotr $1/\sqrt{2}$ is absorbed in $\phi_{A(B)}$ and a new pre-fractor $1/\sqrt{r}$ is extracted out to simplify the subsequent calculations.

The radial equation for the eigenvalue problem $\hat{H}\Psi(\mathbf{r}) = \epsilon\Psi(\mathbf{r})$ is

$$\begin{pmatrix} \epsilon + g/r & -(\partial_r + j/r) \\ (\partial_r - j/r) & \epsilon + g/r \end{pmatrix} \begin{pmatrix} \phi_A \\ \phi_B \end{pmatrix} = 0. \tag{2.49}$$

After diagonalization, the eigenstates are the linear combinations of

$$\phi(r) = \sum_{\lambda=\pm} C_\lambda u_\lambda f_\lambda(r), \qquad u_\pm = \frac{1}{2|j|} \begin{pmatrix} \sqrt{j \pm \alpha} \\ s_{gj}\sqrt{j \mp \alpha} \end{pmatrix}, \tag{2.50}$$

where $s_{gj} = \mathrm{sgn}(gj)$, $\alpha = \sqrt{j^2 - g^2}$, and f_λ satisfies

$$\partial_r^2 f_\lambda(r) + \left[\epsilon^2 + \frac{2g\epsilon}{r} - \frac{\alpha(\alpha - \lambda)}{r^2} \right] f_\lambda(r) = 0. \tag{2.51}$$

Introducing $\rho = |\epsilon|r$, Eq. 2.51 becomes the radial equation for the 3D Coulomb problem [11]. Notice that when $g > g_c = 1/2$, the parameter α in Eq. 2.51 becomes imaginary for some angular momentum channels. The solution to Eq. 2.51 becomes drastically different, which has significant consequences.

2.3.1 Electronic Response in the Sub-critical Region

The sub-critical region is the region where $g < g_c$. In this region, the solution of Eq. 2.51 are in terms of Coulomb wave functions, $F_L(\eta, \rho)$, $G_L(\eta, \rho)$. Letting $\tilde{g} = s_\epsilon g$, the solution to Eq. 2.51 is

$$\phi(r) = \mathscr{N}(u_+ F_{\alpha-1}(-\tilde{g}, \rho) + s_{\epsilon g} u_- F_\alpha(-\tilde{g}, \rho)), \tag{2.52}$$

where the irregular solution at the origin is discarded. The normalization factor $\mathscr{N}$ is determined by imposing orthogonality condition

$$\int \psi_i(\epsilon, r)^\dagger \psi_j(\epsilon, r) dr = \delta_{ij}\delta(\epsilon - \epsilon'), \tag{2.53}$$

which gives

$$\mathscr{N}^2 = \frac{j^2}{2\pi^2\alpha^2}. \tag{2.54}$$

With this solution, the local density of state (LDOS) is

$$N(\epsilon, r) = \sum_{j=-\infty}^{\infty} n_j(\epsilon, r) = \sum_E |\Psi_E(r)|^2 \delta(\epsilon - E). \tag{2.55}$$

Since

$$n_j(\epsilon, r) = \frac{1}{r}|\phi_A(r)|^2 + \frac{1}{r}|\phi_B(r)|^2, \tag{2.56}$$

the contribution of each angular momentum channel is [2]

$$n_j(\epsilon, r) = \frac{N^2}{r}\left[F_{\alpha-1}^2 + F_\alpha^2 + 2\tilde{g}\frac{F_\alpha F_{\alpha-1}}{|j|}\right]. \tag{2.57}$$

The graph of LDOS is

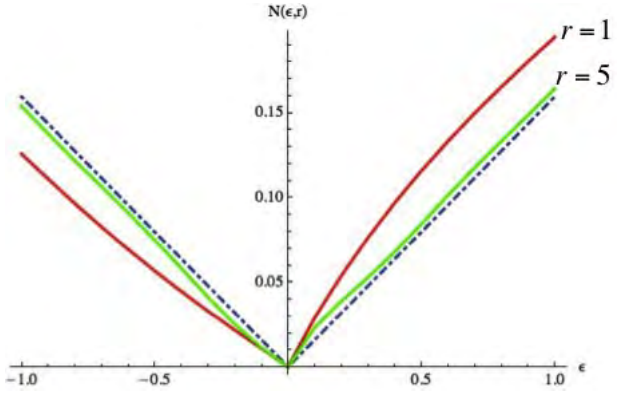

Figure 2.3: Comparison of the LDOS (solid) at different distances (in units of Bohr radius a_0), with an impurity strength of $g = 1/6$. The density of states for $g = 0$ is also included (dotted-dashed).

It is observed that the density of states (DOS) at the positive energy range, which is the density of electron states, is higher than that without an attractive Coulomb potential. Correspondingly, the density of hole states is lower than that at $g = 0$. This is reasonable and intuitive. Since the Coulomb potential introduced in the Hamiltonian is attractive, electrons are attracted to the impurity, resulting in a higher density of electron states. Conversely, holes are repelled from the impurity and the density of hole states is lower. As the distance from the impurity becomes larger, the effect of the attractive potential diminishes. Thus the density of both electron and hole states should approach the case without any potential.

2.3.2 Electronic Response in the Super-critical Region

When $g > g_c$, $\alpha = \sqrt{j^2 - g^2}$ becomes imaginary for some j's and a new parameter $\beta = -i\alpha$ is introduced for these j's. In the sub-critical case, the irregular solution at the origin was discarded. But in the super-critical case, all solutions are regular at the origin, and the solution to ϕ_j comprises of two linearly independent solutions to Eq. 2.51. One is

$$\bar{\phi}_{i\beta}(r) = \bar{u}_+ F_{i\beta-1}(-\tilde{g}, \rho) + s_{jg\epsilon}\bar{u}_- F_{i\beta}(-\tilde{g}, \rho), \tag{2.58}$$

where

$$\bar{u}_{\pm} = \frac{1}{2|g|} \begin{pmatrix} \sqrt{j \pm i\beta} \\ s_g \sqrt{j \mp i\beta} \end{pmatrix}. \tag{2.59}$$

The other solution is simply $\bar{\phi}_{-i\beta}$. The general solution is the linear combination of the both

$$\bar{\phi}_j(r) = C_1 \bar{\phi}_{i\beta}(r) + C_2 \bar{\phi}_{-i\beta}(r), \tag{2.60}$$

where $C_{1,2}$ are determined by the boundary conditions. Since the impurity atom has a certain radius, it is impossible for electrons to penetrate beyond that length scale. Thus we can choose this as a natural cut-off. This boundary condition gives $C_1/C_2 = \exp(2i\delta_j(\epsilon))$, with

$$e^{(i2\delta_j(\epsilon))} = \left(s_g \frac{F_{-i\beta-1} - s_{\epsilon j} F_{-i\beta}}{F_{i\beta-1} - s_{\epsilon j} F_{\beta}} \right)_{\rho=\epsilon a_0} \tag{2.61}$$

By following the same procedures in the sub-critical region, the LDOS from super-critical j's is obtained [2],

$$\bar{n}_j(\epsilon, r) = \frac{1}{2\pi^2 r} \frac{K_j^I(\rho) + s_{\epsilon j} \mathrm{Re}[e^{i2\delta_j} K_j^{II}(\rho)]}{\langle K_j^I(\infty) + s_{\epsilon j} \mathrm{Re}[e^{i2\delta_j} K_j^{II}(\infty)] \rangle_r}, \tag{2.62}$$

where the

$$K_j^I = |F_{i\beta}|^2 + |F_{i\beta-1}|^2 + \frac{2|j|}{\tilde{g}} \mathrm{Re}\left[F_{i\beta} F_{-i\beta-1}\right], \tag{2.63}$$

$$K_j^{II} = 2F_{i\beta} F_{i\beta-1} + \frac{|j|}{\tilde{g}} \left(F_{i\beta}^2 + F_{i\beta-1}^2\right) \tag{2.64}$$

and the $\langle \cdots \rangle_r$ refers to the term as $r \to \infty$. The total LDOS of all j's channels is

$$N(\epsilon, r) = \sum_{|j|>|g|} n_j(\epsilon, r) + \sum_{|j|<|g|} \bar{n}_j(\epsilon, r). \tag{2.65}$$

The LDOS of state in the super-critical region is shown below

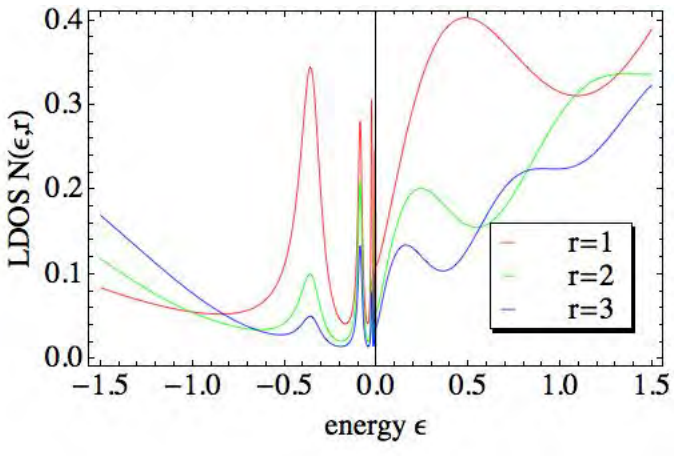

Figure 2.4: Comparison of the LDOS (solid) at different distances (in units of lattice spacing a), with an impurity strength of $g = 4/3$.

From Fig. 2.4, we can see that strong resonant states appear in the hole region. Intuitively, this resonant peak becomes weaker as the distance from the impurity gets larger. A density plot of the hole region is shown in Fig. 2.5.

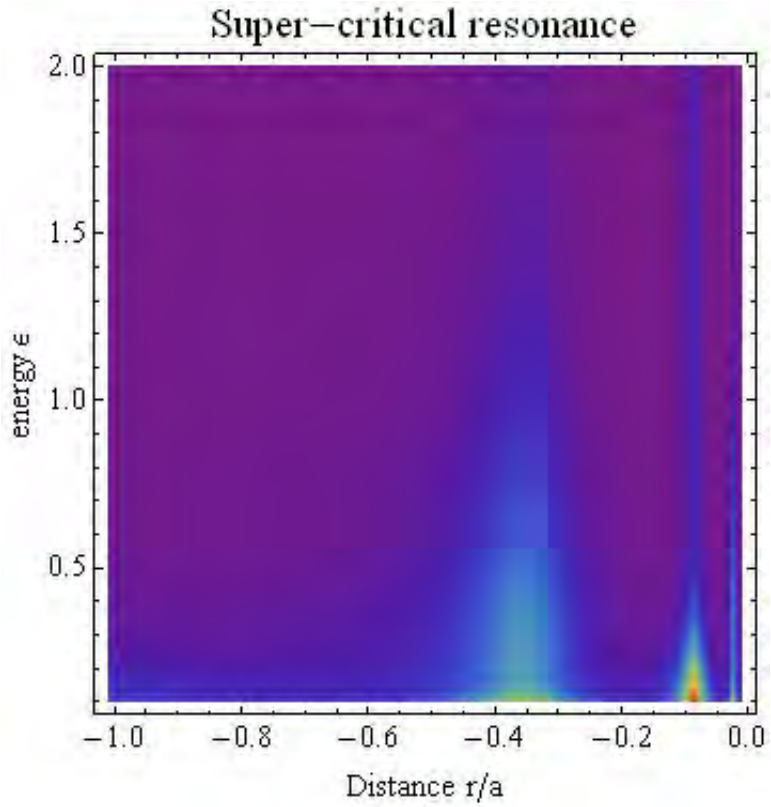

Figure 2.5: The density plot of the LDOS in the hole region for different ϵ and r. The super-critical atomic collapse is seen clearly for small r.

As the resonance peak occurs in the hole region for an attractive potential, the density plot only includes the hole region ($\epsilon < 0$). The signature for resonance is very prominent at small distance and its strength gradually diminishes as r goes larger. Notice that the LDOS makes fast oscillations in the vicinity of the impurity. This is another signature of super-critical region as the asymptotic solution near the impurity ($r \to 0$) acquires an imaginary exponential dependence $\bar{\phi}_j(0) \sim r^{i\beta}$.

2.4 Experimental Proof and Motivation

Recently, Wang *et al.* has successfully demonstrated the existence of this super-critical resonance state in graphene [4]. The experiment used Ca dimers as the impurity atoms and maneuvered the impurity atoms to form an impurity cluster on a graphene surface. This impurity cluster behaves like a single impurity atom of a greater strength, and thus induces the super-critical response of electrons in graphene. The LDOS is directly proportional to the dI/dV curve, which could be measured in the scanning tunneling microscope (STM). Hence it is possible to deduce the behavior of LDOS in the super-critical region by the STM measurements. Their STM measurement and the theoretical prediction are shown below.

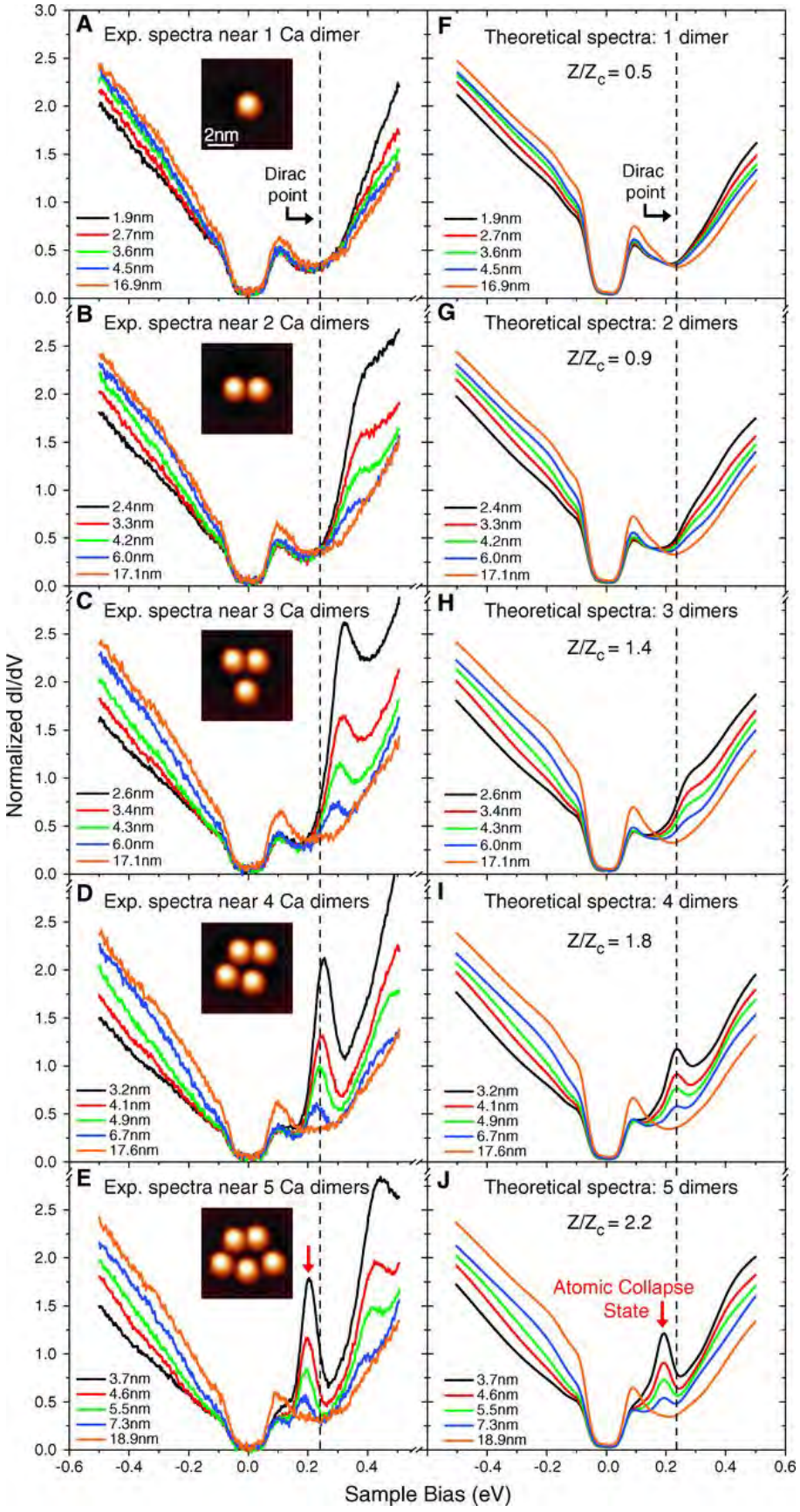

Figure 2.6: Left panels: experimental scanning tunneling microscopic data of the LDOS of graphene at different impurity strengths. Right panels: the corresponding theoretical prediction. Adapted from [4].

The broad dip on the left of the resonance peak was due to the substrate effect and was accounted for in the theoretical prediction. A strong resonance peak develops in the hole region with the impurity strength. This peak is the primary feature that confirms the existence of the super-critical atomic collapse and has ignited new interest on this decade-old quest.

Notice that from Panel H of Fig. 2.6, the onset of the super-critical atomic collapse occurs at an effective impurity strength of $Z = 1.4Z_c$, where Z_c is the theoretical threshold. This large effective impurity strength needed for super-critical regime presents a non-trivial issue. This has indeed motivated me to search for a way to reduce the impurity strength required, thus being able to control the super-critical collapse.

The coupling constant for the impurity in a medium is

$$g = \frac{Ze^2}{4\pi\epsilon_0\epsilon v_F}, \tag{2.66}$$

where the newly introduced parameter ϵ is the dielectric constant. It is generally larger than unity, thereby reducing the coupling strength. One of the contributions to this dielectric constant ϵ is the electron-electron (e-e) interaction in the material. Thus the effective impurity strength could be enhanced if the e-e interaction is suppressed.

Potentially, one method to suppress the e-e interaction is to apply a magnetic field. Under a magnetic field, the energy spectrum of graphene discretizes into levels, which are called "Landau levels". This discretization creates energy gaps and no energy states are available at energies in the energy gap. Hence the electron will not interact with each other unless the final energy states are not in the energy gaps. In this way, the e-e interaction could be greatly reduced. Thus by controlling the magnetic field, one is expected to be able to control whether the system is in sub- or super-critical region.

The goal of this thesis is to attempt to extract an analytical solution of electronic response in the super-critical region under a strong magnetic field. If an analytical solution is not available, a numerical solution should be obtained to investigate the effect of a magnetic field on the super-critical region.

Chapter 3

Landau Levels in Grahene

Before considering the effect of a magnetic field on the electrons near a Coulomb impurity, this chapter studies only the electron behavior in a magnetic field, which are the Landau levels. At the end of this chapter, a weak Coulomb impurity is added to the Landau level energy spectrum in an effort to establish a limiting case for reference.

3.1 2D Dirac fermions under a constant magnetic field

3.1.1 Set-up

For the case of an electron $q = -e$ in a uniform magnetic field $\mathbf{B} = B\hat{\mathbf{e}}_z$ in a symmetric gauge $\mathbf{A} = -\frac{1}{2}\mathbf{r} \times \mathbf{B}$, the kinetic momentum operator is defined as,

$$\hat{\boldsymbol{\pi}} = m\hat{\mathbf{v}} = \hat{\mathbf{p}} + e\hat{\mathbf{A}}. \tag{3.1}$$

Since [12]

$$[\hat{\pi}_x, \hat{\pi}_y] = m^2[\hat{v}_x, \hat{v}_y] = -i\hbar eB_z = -i\frac{\hbar^2}{l_B^2}, \qquad [\hat{\pi}_x, \hat{\pi}_z] = [\hat{\pi}_y, \hat{\pi}_z] = 0, \tag{3.2}$$

where $l_B = \sqrt{\hbar/(eB)}$ is the magnetic length.

3.1.2 Non-relativistic Free Particle in a magnetic field

The Hamiltonian of a 2D free Schrödinger particle in a magnetic field is given by $\hat{H}_S$,

$$\begin{aligned} \hat{H}_S &= \frac{\hat{\pi}_x^2 + \hat{\pi}_y^2}{2m} = \frac{\left(\hat{\mathbf{p}} + e\hat{\mathbf{A}}\right)^2}{2m} = \frac{(\hat{p}_x + e\hat{A}_x)^2 + (\hat{p}_y + e\hat{A}_y)^2}{2m} && (3.3) \\ &= \frac{(\hat{p}_x - \frac{eB}{2}\hat{y})^2 + (\hat{p}_y + \frac{eB}{2}\hat{x}_y)^2}{2m} && (3.4) \\ &= \frac{\hbar\omega_c}{2}(\hat{Q}^2 + \hat{S}^2), && (3.5) \end{aligned}$$

where $\omega_c = eB/m$ with

$$\hat{Q} = \sqrt{\frac{1}{\hbar\omega_c m}}\hat{\pi}_y, \qquad \hat{S} = \sqrt{\frac{1}{\hbar\omega_c m}}\hat{\pi}_y, \qquad [\hat{Q}, \hat{S}] = i. \tag{3.6}$$

The annihilation operator $\hat{a}$ and the creation operator $\hat{a}^\dagger$ are defined as

$$\hat{a} = \frac{1}{\sqrt{2}}\left(\hat{Q} + i\hat{S}\right), \qquad \hat{a}^\dagger = \frac{1}{\sqrt{2}}\left(\hat{Q} - i\hat{S}\right), \tag{3.7}$$

such that

$$\begin{aligned} \left[\hat{a}, \hat{a}^\dagger\right] &= i\frac{l_B^2}{\hbar^2}\left[\hat{\pi}_x, \hat{\pi}_y\right] = 1, && (3.8) \\ \hat{a}^\dagger|n\rangle &= \sqrt{n+1}|n+1\rangle, && (3.9) \\ \hat{a}|n\rangle &= \sqrt{n}|n\rangle. && (3.10) \end{aligned}$$

With the newly defined creation and annihilation operators, the momentum operators are expressed as

$$\hat{\pi}_x = \frac{\hbar}{i\sqrt{2l_B^2}}\left(\hat{a} - \hat{a}^\dagger\right), \qquad \hat{\pi}_y = \frac{\hbar}{\sqrt{2l_B^2}}\left(\hat{a} + \hat{a}^\dagger\right). \tag{3.11}$$

Thus the Hamiltonian can be written as

$$\hat{H}_S = \frac{\hbar\omega_c}{2}\left(2\hat{a}^\dagger\hat{a} + 1\right) = \hbar\omega_c\left(\hat{a}^\dagger\hat{a} + \frac{1}{2}\right), \tag{3.12}$$

with an eigen-energy as

$$\epsilon_S = \hbar\omega_c \left(n + \frac{1}{2}\right) = \frac{\hbar eB}{m}\left(n + \frac{1}{2}\right). \tag{3.13}$$

3.1.3 Relativistic Free Particle in a magnetic field

The Hamiltonian of a 2D free Dirac particle in a magnetic field is given by $\hat{H}_D$,

$$\begin{aligned}
\hat{H}_D &= v_F \boldsymbol{\sigma} \cdot \left(\hat{\mathbf{p}} + e\hat{\mathbf{A}}\right) = v_F \boldsymbol{\sigma} \cdot \hat{\boldsymbol{\pi}} && (3.14)\\
&= v_F \begin{pmatrix} 0 & \hat{\pi}_x - i\hat{\pi}_y \\ \hat{\pi}_x + i\hat{\pi}_y & 0 \end{pmatrix} && (3.15)\\
&= \hbar\omega_c' \begin{pmatrix} 0 & -\hat{a} \\ \hat{a}^\dagger & 0 \end{pmatrix}, && (3.16)
\end{aligned}$$

where $\omega_c' = \sqrt{2}v_F/l_B$. This gives

$$\begin{aligned}
H_D\psi_n &= \epsilon_n\psi_n, && (3.17)\\
\hbar\omega_c' \begin{pmatrix} 0 & -i\hat{a} \\ i\hat{a}^\dagger & 0 \end{pmatrix} \begin{pmatrix} F_n \\ G_n \end{pmatrix} &= \epsilon_n \begin{pmatrix} F_n \\ G_n \end{pmatrix}. && (3.18)
\end{aligned}$$

Solving this eigenvalue problem, we obtain the eigen-energy,

$$\epsilon_n = \pm\hbar\omega_c' = \pm\sqrt{2\hbar e v_F^2 B n} = \pm\sqrt{2n}\frac{\hbar v_F}{l_B}. \tag{3.19}$$

The eigen-state is

$$\psi_n = \begin{pmatrix} F_n \\ G_n \end{pmatrix} = \frac{1}{\sqrt{2}} \begin{pmatrix} |n-1\rangle \\ \mp i|n\rangle \end{pmatrix}. \tag{3.20}$$

In particular,

$$\psi_{n=0} = \begin{pmatrix} 0 \\ |n=0\rangle \end{pmatrix} \tag{3.21}$$

3.2 Level Degeneracy in Landau Levels

The Hamiltonians of both the Schrödinger particle and the Dirac particle are

$$\hat{H}_S = \frac{\left(\hat{\mathbf{p}} + e\hat{\mathbf{A}}\right)^2}{2m} = \frac{\left(\hat{p}_x - \frac{eB}{2}\hat{y}\right)^2 + \left(\hat{p}_y + \frac{eB}{2}\hat{x}\right)^2}{2m} \tag{3.22}$$

$$\hat{H}_D = v_F \boldsymbol{\sigma} \cdot \left(\hat{\mathbf{p}} + e\hat{\mathbf{A}}\right) = v_F \left[\sigma_x \left(\hat{p}_x - \frac{eB}{2}\hat{y}\right) + \sigma_y \left(\hat{p}_y + \frac{eB}{2}\hat{x}\right)\right]. \tag{3.23}$$

Both Hamiltonians depend on two pairs of conjugate operator $(\hat{p}_x,\ \hat{x})$ & $(\hat{p}_y,\ \hat{y})$. After expressing them in terms of creation and annihilation operators, $\hat{H}_S$ & $\hat{H}_D$ only depend on 1 pair of conjugate operators $\left(\hat{a},\ \hat{a}^\dagger\right)$. It is thus important to search for a second pair of conjugate operators, which necessarily commutes with the Hamiltonian and gives rise to the level degeneracy of Landau levels.

Analogue to $\hat{\boldsymbol{\pi}} = \hat{\mathbf{p}} + e\hat{\mathbf{A}}$, consider $\hat{\underset{\sim}{\pi}} = \hat{\mathbf{p}} - e\hat{\mathbf{A}}$ with

$$\left[\hat{\underset{\sim}{\pi}}_x, \hat{\underset{\sim}{\pi}}_y\right] = i\frac{\hbar^2}{l_B^2} = \left[\hat{\pi}_x, \hat{\pi}_y\right]. \tag{3.24}$$

Combining the two gives

$$\hat{\mathbf{p}} = \frac{1}{2}\left(\hat{\pi} + \hat{\underset{\sim}{\pi}}\right), \qquad \hat{\mathbf{A}} = \frac{1}{2e}\left(\hat{\pi} - \hat{\underset{\sim}{\pi}}\right). \tag{3.25}$$

Following the same procedures, the conjugate creation and annihilation operators are

$$\hat{b} = \frac{l_B}{\sqrt{2}\hbar}\left(\hat{\underset{\sim}{\pi}}_y + i\hat{\underset{\sim}{\pi}}_x\right), \qquad \hat{b}^\dagger = \frac{l_B}{\sqrt{2}\hbar}\left(\hat{\underset{\sim}{\pi}}_y - i\hat{\underset{\sim}{\pi}}_x\right), \tag{3.26}$$

such that

$$\left[\hat{b}, \hat{b}^\dagger\right] = 1, \qquad \left[\hat{b}, \hat{a}\right] = \left[\hat{b}^\dagger, \hat{a}\right] = \left[\hat{b}, \hat{a}^\dagger\right] = \left[\hat{b}^\dagger, \hat{a}^\dagger\right] = 0. \tag{3.27}$$

Note that

$$\hat{\underset{\sim}{\pi}}_x = \frac{\hbar}{i\sqrt{2}l_B}\left(\hat{b} - \hat{b}^\dagger\right), \qquad \hat{\underset{\sim}{\pi}}_y = \frac{\hbar}{\sqrt{2}l_B}\left(\hat{b} + \hat{b}^\dagger\right). \tag{3.28}$$

One may introduce

$$\hat{b}^\dagger \hat{b}|m\rangle = m|m\rangle, \tag{3.29}$$

so that the quantum states become the tensor product of the two Hilbert spaces $|n\rangle$ and $|m\rangle$. For non-relativistic particle, the complete eigen-state is

$$|n,m\rangle = |n\rangle \otimes |m\rangle = \frac{(\hat{a}^\dagger)^n}{\sqrt{n!}} \frac{(\hat{b}^\dagger)^m}{\sqrt{m!}} |n=0, m=0\rangle. \tag{3.30}$$

For the Dirac fermions in graphene, the complete eigenstates are

$$\begin{aligned} \psi_{n,m}(\mathbf{r}) &= \langle \mathbf{r}| \left[\frac{1}{\sqrt{2}} \begin{pmatrix} |n-1\rangle \\ \mp i|n\rangle \end{pmatrix} \otimes |m\rangle \right] \\ &= \frac{1}{\sqrt{2}} \begin{pmatrix} \langle \mathbf{r}|n-1,m\rangle \\ \mp i\langle \mathbf{r}|n,m\rangle \end{pmatrix} = \frac{1}{\sqrt{2}} \begin{pmatrix} \phi_{n-1,m}(\mathbf{r}) \\ \mp i\phi_{n,m}(\mathbf{r}) \end{pmatrix}, \end{aligned} \tag{3.31}$$

$$\begin{aligned} \psi_{n=0,m} &= \langle \mathbf{r}| \left[\begin{pmatrix} 0 \\ |n\rangle \end{pmatrix} \otimes |m\rangle \right] \\ &= \begin{pmatrix} 0 \\ \langle \mathbf{r}|n=0,m\rangle \end{pmatrix} = \begin{pmatrix} 0 \\ \phi_{0,m}(\mathbf{r}) \end{pmatrix}. \end{aligned} \tag{3.32}$$

3.2.1 Semi-classical interpretation of level degenracy

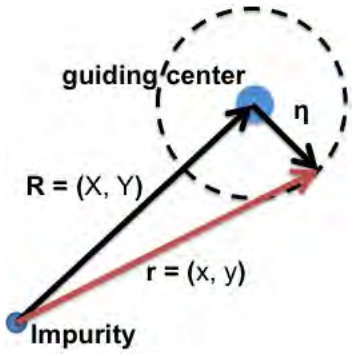

Figure 3.1: A schematic of the cyclotron motion of electrons in a magnetic field. The distance of the guiding centre to the impurity is proportional to the quantum number m and the cyclotron radius is proportional to the quantum number n.

To understand level degeneracy, we come back to the equation of motion of an electron in a magnetic field,

$$m\frac{d^2\hat{\mathbf{r}}}{dt^2} = -e\frac{d\hat{\mathbf{r}}}{dt} \times \mathbf{B}. \tag{3.33}$$

Integration of $d^2\hat{\mathbf{r}}/dt^2$ gives

$$\frac{d\hat{x}}{dt} = \frac{\hat{\pi}_x}{m} = -\omega_c\left(\hat{y} - \hat{Y}\right), \qquad \frac{d\hat{y}}{dt} = \frac{\hat{\pi}_y}{m} = \omega_c\left(\hat{x} - \hat{X}\right). \tag{3.34}$$

By rewriting the equations above, the solutions to $\hat{x}$ and $\hat{y}$ are

$$\hat{x} = \hat{X} + \frac{\hat{\pi}_y}{eB}, \qquad \hat{y} = \hat{Y} - \frac{\hat{\pi}_x}{eB}. \tag{3.35}$$

To relate the position of the guiding center $\hat{\mathbf{R}}$ to the pseudo-momentum $\hat{\underset{\sim}{\boldsymbol{\pi}}}$ in the symmetric gauge consider

$$e\hat{\mathbf{A}} = \frac{eB}{2}\begin{pmatrix} -\hat{y} \\ \hat{x} \end{pmatrix} = \frac{1}{2}\left(\hat{\boldsymbol{\pi}} - \hat{\underset{\sim}{\boldsymbol{\pi}}}\right) = \frac{1}{2}\begin{pmatrix} \hat{\pi}_x - \hat{\underset{\sim}{\pi}}_x \\ \hat{\pi}_y - \hat{\underset{\sim}{\pi}}_y \end{pmatrix}, \tag{3.36}$$

which gives

$$\hat{X} = -\frac{\hat{\underset{\sim}{\pi}}_y}{eB}, \qquad \hat{Y} = \frac{\hat{\underset{\sim}{\pi}}_x}{eB}. \tag{3.37}$$

With the understanding that $\hat{\mathbf{r}} = \hat{\mathbf{R}} + \hat{\boldsymbol{\eta}}$, the radius of cyclotron motion $\hat{\boldsymbol{\eta}}$ is

$$\hat{\eta}_x = \frac{\hat{\pi}_y}{eB}, \qquad \hat{\eta}_y = \frac{\hat{\pi}_x}{eB}. \tag{3.38}$$

Thus the real momentum $\hat{\boldsymbol{\pi}}$ is related to (up to a proportionality factor) the radius of cyclotron motion $\hat{\boldsymbol{\eta}}$, and the pseudo-momentum $\hat{\underset{\sim}{\boldsymbol{\pi}}}$ is related to the position of the guiding center $\hat{\mathbf{R}}$.

For degeneracy, notice that

$$\left[\hat{X}, \hat{Y}\right] = \frac{1}{(eB)^2}\left[-\hat{\underset{\sim}{\pi}}_y, \hat{\underset{\sim}{\pi}}_x\right] = il_B^2. \tag{3.39}$$

This means it is impossible to know both $\hat{\mathbf{X}}$ and $\hat{\mathbf{Y}}$ precisely at the same time. The guiding center therefore smears over a surface area

$$\Delta\mathbf{X}\Delta\mathbf{Y} = 2\pi l_B^2. \tag{3.40}$$

The number of degenerate states per unit area is thus

$$n = \frac{1}{2\pi l_B^2} = \frac{B}{\phi_0}, \tag{3.41}$$

where $\phi_0 = h/e$ is the flux quantum.

3.3 Eigenstates in Landau Levels

From the previous results

$$|n, m\rangle = \frac{(\hat{a}^\dagger)^n}{\sqrt{n!}} \frac{(\hat{b}^\dagger)^m}{\sqrt{m!}} |n = 0, m = 0\rangle \tag{3.42}$$

$$\hat{a}|n = 0, m\rangle = 0, \tag{3.43}$$

let

$$z = x - iy = re^{-i\theta}, \qquad \bar{z} = x + iy = re^{+i\theta}, \tag{3.44}$$

$$\partial = \frac{1}{2}\left(\partial_x + i\partial_y\right) \qquad \bar{\partial} = \frac{1}{2}\left(\partial_x - i\partial_y\right), \tag{3.45}$$

such that

$$\partial z = 1, \qquad \partial\bar{z} = 0, \qquad \bar{\partial}z = 0, \qquad \bar{\partial}\bar{z} = 1. \tag{3.46}$$

The creation and annihilation operators can then be expressed in terms of these variables,

$$\hat{a} = \sqrt{2}\left[\frac{l_b}{2}\left(\partial_x - i\partial_y\right) + \frac{x-iy}{4l_B}\right] = \sqrt{2}\left(\frac{z}{4l_B} + l_B\bar{\partial}\right), \tag{3.47}$$

$$\hat{a}^\dagger = -\sqrt{2}\left(\frac{\bar{z}}{4l_B} - l_B\partial\right), \tag{3.48}$$

$$\hat{b} = \sqrt{2}\left(\frac{\bar{z}}{4l_B} + l_B\partial\right), \tag{3.49}$$

$$\hat{a}^\dagger = -\sqrt{2}\left(\frac{z}{4l_B} - l_B\bar{\partial}\right). \tag{3.50}$$

Eq. 3.43 in terms of the new variables is

$$\sqrt{2}\left(\frac{z}{4l_B} + l_B\bar{\partial}\right)\phi_{n=0}(z,\bar{z}) = 0, \tag{3.51}$$

where $\phi_{n,m}(\mathbf{r}) = \langle \mathbf{r}|n,m\rangle$. The solution is

$$\phi_{n=0}(z,\bar{z}) = f(z)\exp\left[-\frac{|z|^2}{4l_B^2}\right]. \tag{3.52}$$

Similarly for $\hat{b}|n,m=0\rangle = 0$,

$$\phi_{m=0}(z,\bar{z}) = g(\bar{z})\exp\left[-\frac{|z|^2}{4l_B^2}\right]. \tag{3.53}$$

By combining the two, the solution is

$$\phi_{n=0,m=0}(z,\bar{z}) = \frac{1}{\sqrt{2\pi l_B^2}}\exp\left[-\frac{|z|^2}{4l_B^2}\right]. \tag{3.54}$$

One can obtain the solution for any arbitrary pair of (n,m) by repeatedly applying $\hat{a}^\dagger$ and $\hat{b}^\dagger$ to $\phi_{n=0,m=0}(z,\bar{z})$. The general solution is

$$\begin{aligned}\phi_{n,m}(z,\bar{z}) &= \frac{1}{\sqrt{2\pi l_B^2}}\frac{(-1)^n\sqrt{2}^n}{n!}\frac{(-1)^m\sqrt{2}^m}{m!}\left(\frac{\bar{z}}{4l_B} - l_B\partial\right)^n\left(\frac{z}{4l_B} - l_B\bar{\partial}\right)^m\exp\left[-\frac{|z|^2}{4l_B^2}\right] \\ &= \frac{(-1)^m\exp\left(-\frac{|z|^2}{4l_B^2}\right)}{\sqrt{2\pi l_B^2}}\sqrt{\frac{n!}{m!}}\left(\frac{z}{\sqrt{2\pi l_B^2}}\right)^{m-n}L_n^{m-n}\left(-\frac{|z|^2}{2l_B^2}\right),\end{aligned} \tag{3.55}$$

where $L_n^{m-n}\left(-\frac{|z|^2}{2l_B^2}\right)$ is the generalized Laguerre polynomial. Expressed in terms of r and

θ, Eq. 3.55 becomes

$$\phi_{n,m}(\mathbf{r}) = \frac{(-1)^m \exp\left(-\frac{r^2}{4l_B^2}\right)}{\sqrt{2\pi l_B^2}} \sqrt{\frac{n!}{m!}} \left(\frac{re^{-i\theta}}{\sqrt{2\pi l_B^2}}\right)^{m-n} L_n^{m-n}\left(-\frac{r^2}{2l_B^2}\right). \quad (3.56)$$

We verify that the eigenstates are orthogonal to one another by

$$\int_0^{2\pi}\int_0^{\infty} \phi_{n,m}\phi^*_{n',m'} r dr d\theta = \delta_{n,n'}\delta_{m,m'}. \quad (3.57)$$

Plots of some particular eigenstates are shown below.

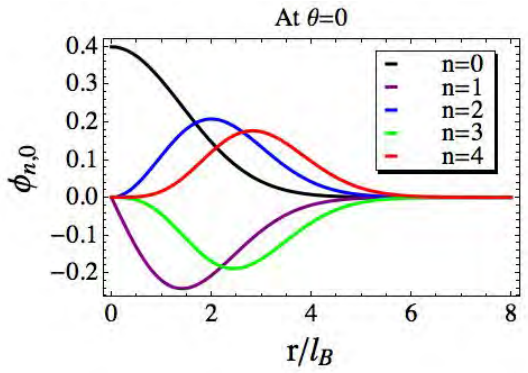

Figure 3.2: Eigenstates of Landau levels at a fixed $m = 0$ for different n, $n = 0, 1, 2, 3, 4$.

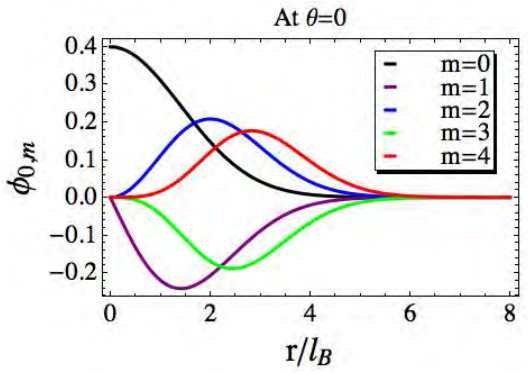

Figure 3.3: Eigenstates of Landau levels at a fixed $n = 0$ for different m, $m = 0, 1, 2, 3, 4$.

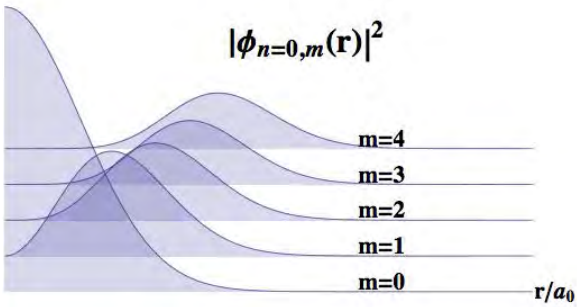

Figure 3.4: The probability of $|\phi|^2$ at a fixed $n = 0$ and different m, $m = 0, 1, 2, 3, 4$.

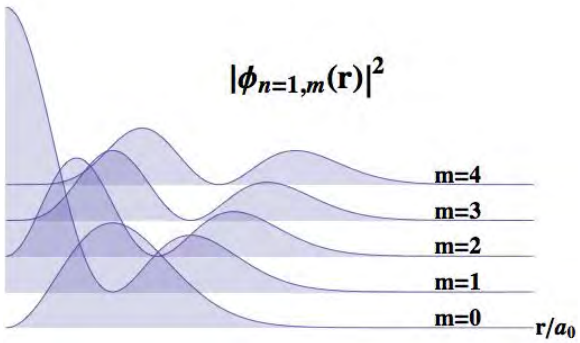

Figure 3.5: The probability of $|\phi|^2$ at a fixed $n = 1$ and different m, $m = 0, 1, 2, 3, 4$.

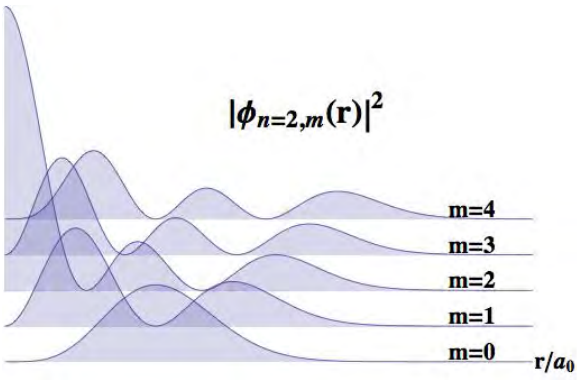

Figure 3.6: The probability of $|\phi|^2$ at a fixed $n = 2$ and different m, $m = 0, 1, 2, 3, 4$.

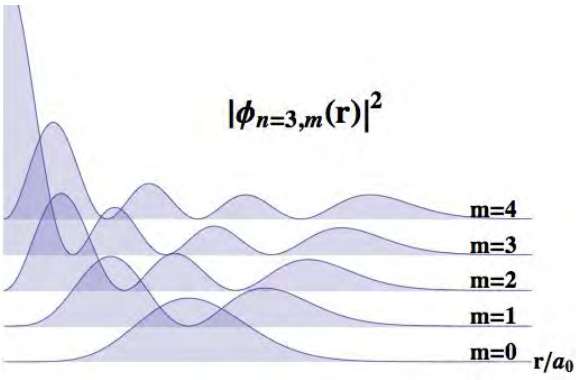

Figure 3.7: The probability of $|\phi|^2$ at a fixed $n = 3$ and different m, $m = 0, 1, 2, 3, 4$.

There are several characteristic features from these figures which could be generalized to all n and m. Firstly, the wave functions are symmetric about quantum number n and m as shown in Fig. 3.2 and 3.3. This is a consequence of the fact that $\hat{a}^\dagger$ commutes with $\hat{b}^\dagger$. Secondly, Fig. 3.4 to 3.7 show that the probability functions are independent of the azimuth angle θ which follows from the symmetric gauge used. Thirdly, the spectral weights of the wave functions for a fixed n shift away from the origin with increasing m for a fixed $n = 0$. In fact, a closer inspection reveals that the spectral weights of the wave functions for a fixed n first shift towards the origin from $m = 0$ to $m = n - 1$, center at origin for $m = n$, and then shift away from the origin from $m = n + 1$ to $m = \infty$.

3.4 Perturbation to Landau Levels

We consider now a time-independent scalar potential as a perturbation to the Hamiltonian of a Dirac particle in the presence of a constant magnetic field

$$\hat{H} \;=\; v_F \boldsymbol{\sigma} \cdot \left(\hat{\mathbf{p}} + e\hat{\mathbf{A}}\right) + \left(-\frac{g}{r}\right). \tag{3.58}$$

The wave function of a Dirac particle in a magnetic field without perturbation is

$$\psi_{n,m}(\mathbf{r}) \;=\; \frac{1}{\sqrt{2}} \begin{pmatrix} \langle \mathbf{r}|n-1,m\rangle \\ \mp i\langle \mathbf{r}|n,m\rangle \end{pmatrix} = \frac{1}{\sqrt{2}} \begin{pmatrix} \phi_{n-1,m}(\mathbf{r}) \\ \mp i\phi_{n,m}(\mathbf{r}) \end{pmatrix}. \tag{3.59}$$

Following the time-independent degenerate perturbation theory, the first order correction to energy $\Delta\epsilon_{n,m}$ of nth Landau level is derived by obtaining the eigenvalue of the matrix whose elements are

$$\langle\psi_{n,m}|\left(-\frac{g}{r}\right)|\psi_{n,m'}\rangle = \frac{1}{2}\left[\langle n-1,m|\left(-\frac{g}{r}\right)|n-1,m'\rangle + \langle n,m|\left(-\frac{g}{r}\right)|n,m'\rangle\right]. \quad (3.60)$$

It is straightforward to show from the integration of the angular components that

$$\langle n,m|\left(-\frac{g}{r}\right)|n',m'\rangle \sim \delta_{n-m,n'-m'}. \quad (3.61)$$

In fact, we can show that

$$\langle n,m|\left(-\frac{g}{r}\right)|n',m'\rangle = \frac{(-1)^{n'+m+m'}(-g)}{\sqrt{2l_B^2}}\sqrt{\frac{n!m!}{n'!m'!}}\frac{\sqrt{\pi}\Gamma(m-n+1/2)}{\Gamma(n+1)\Gamma(1/2-n')\Gamma(m-n+1)}$$
$${}_3F_2\left(\frac{1}{2},m-n+\frac{1}{2},-n;m-n+1,\frac{1}{2}-n';1\right)\delta_{n-m,n'-m'}. \quad (3.62)$$

Thus only the diagonal terms ($m = m'$) in Eq. 3.60 are non-zero. Each diagonal term is the first order energy correction for each m. Thus, Eq. 3.60 becomes

$$\Delta\epsilon_{n,m} = \frac{1}{2}\left[\langle n-1,m|\left(-\frac{g}{r}\right)|n-1,m\rangle + \langle n,m|\left(-\frac{g}{r}\right)|n,m\rangle\right]. \quad (3.63)$$

For example, the energy corrections to the 0^{th} Landau level are shown in Fig. 3.8,

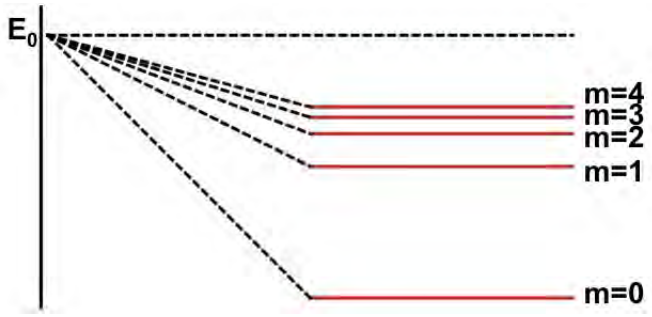

Figure 3.8: An example of the energy splitting at a nonzero g for the 0^{th} Landau level.

We notice that the maximum splitting occurs at $m = n-1$, and is given by $\Delta\epsilon_{n,n-1}$.

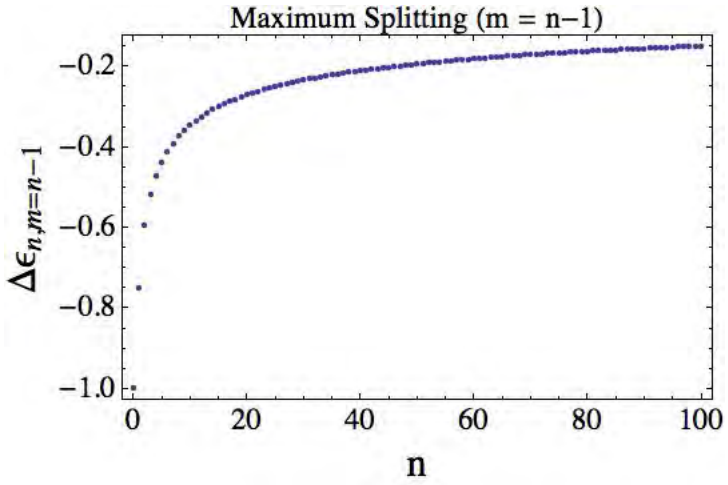

Figure 3.9: A graph of maximum splitting of the energy levels against n.

This is reasonable. As shown in Fig. 3.1, the effect of the impurity is felt the most when an electron is very close to the impurity. This means $\mathbf{r} = 0$ or $\mathbf{R} - \boldsymbol{\eta} = 0$. Shown in Eq. 3.37 and 3.38, the position of of the guiding center $\mathbf{R}$ is related to $\hat{\boldsymbol{\pi}}$ which relates to the quantum number m and the radius of the cyclotron orbit $\boldsymbol{\eta}$ is related to $\hat{\boldsymbol{\pi}}$ which is related to the quantum number n. Therefore, the displacement $\mathbf{r}$ is related to $n-m$. The minimum displacement occurs at $n - m = 0$. In Eq. 3.60, there are two contributions to the energy correction. One is from the $(n-1)^{th}$ state and the other is from the n^{th} state. Since the scalar potential decays following the $1/r$ law from origin to infinity and from Fig. 3.4 to 3.7, the spectral weight of $\phi_{n,m}$ for fixed m moves away from the origin, this implies that the contribution from $(n-1)^{th}$ state to the energy correction is more than that from n^{th} state. Thus, the maximum splitting occurs at $(n-1) - m = 0$ or $m = n - 1$. The maximum splitting slowly decreases to zero when it is sufficiently far from the impurity.

As the matrix is already diagonalized, the corrected eigen-states are the same as the original ones, $\psi_{n,m}(\mathbf{r})$.

The local density of state (LDOS) is given by

$$N(\epsilon, r) = \sum_{n,m} \delta\left(\epsilon - \epsilon_{n,m}\right) |\psi_{n,m}|^2 \approx \sum_{n,m} \frac{\Gamma^2}{\left(\epsilon - \epsilon_{n,m}\right)^2 + \Gamma^2} |\psi_{n,m}|^2, \tag{3.64}$$

where $\epsilon_{n,m} = \epsilon_n + \Delta\epsilon_{n,m}$ and the delta function is approximated by a Lorentzian function to simulate the fact that observations are limited by the resolution of the equipment.

Ideally, the summation in Eq. 3.64 of m for each n should run from zero to infinity. In practice, we generally have a sample of a certain size d. Since spectral weight generally moves further away from the impurity with increasing m, it is reasonable to choose an effective cut-off m such that the contribution to the LDOS from the wave functions outside d is virtually zero. For this requirement to be held effectively, we look for the position r of the first maximum of the m^{th} wave functions such that $r - l_B > d$.

Furthermore, for the ease of viewing, the atomic unit system in which $\hbar = e = 1/(4\pi\epsilon_0) = 1$ and $c \approx 137$ is employed in the calculation. In the atomic unit system the length unit is the Bohr radius (a_0) which is about 0.5 Å, and the energy unit is 1 Hartree (H) which is about 27.2 eV. 1 Tesla of magnetic field is equal to 1/23500 a.u..

3.4.1 Case I: B=1 T

The magnetic length in atomic units at B=1 T is $l_B = \sqrt{\hbar/(eB)} \approx 484$ a_0. To make a plot for a sample size of 4 $l_B \approx 1939$ a_0, the cut-off m is found to be 26, as shown in Fig. 3.10.

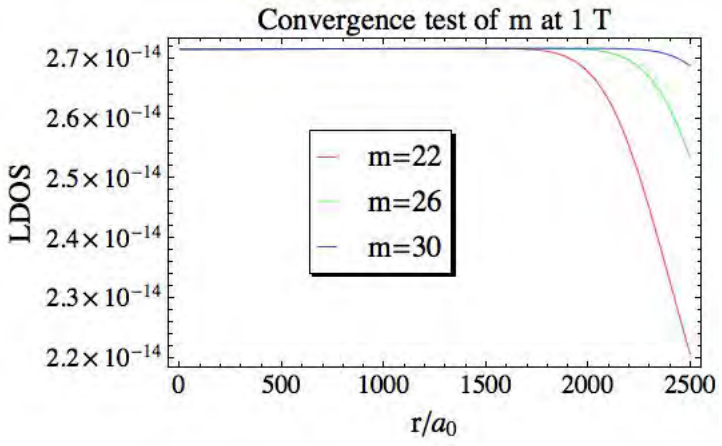

Figure 3.10: A convergence test to determine the appropriate cut-off. For a region of interest of $4l_B \approx 2000$, the best cut-off is at $m = 26$ so that it does miss much contribution from large m's and does not include too many m's to adversely affect the computation time.

A density plot of LDOS of up to the third Landau level ($n = 0, 1, 2, 3$) for a displacement up to 4 l_B at 1 T of B field is shown in Fig. 3.11.

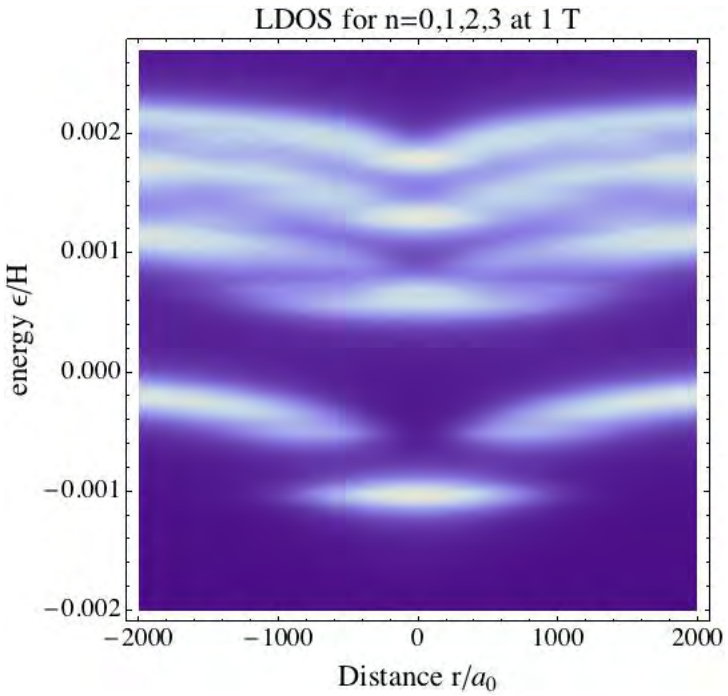

Figure 3.11: A density plot of the LDOS at 1T of the magnetic field, with n = 0 - 3 and m = 0 - 26.

Plots of LDOS at fixed distances ($r = l_B, 2l_B, 3l_B, 4l_B$) at 1 T of B field are shown.

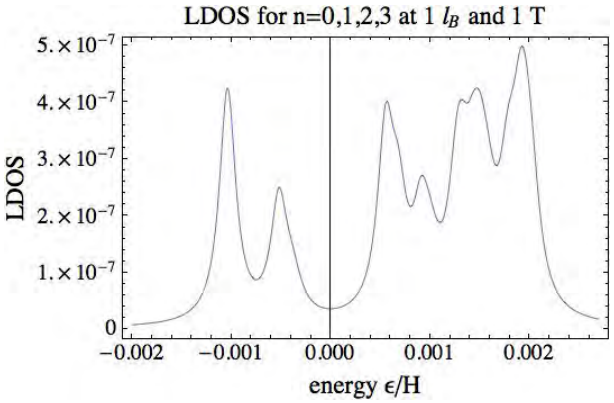

Figure 3.12: A plot of the LDOS at a distance of $1l_B$ from the impurity at 1T, with n = 0 - 3 and m = 0 - 26.

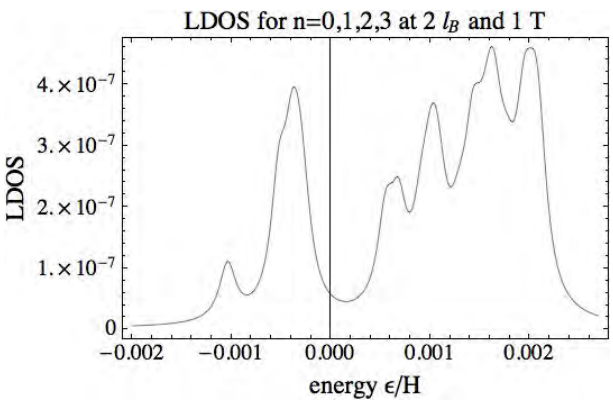

Figure 3.13: A plot of the LDOS at a distance of $2l_B$ from the impurity at 1T, with n = 0 - 3 and m = 0 - 26.

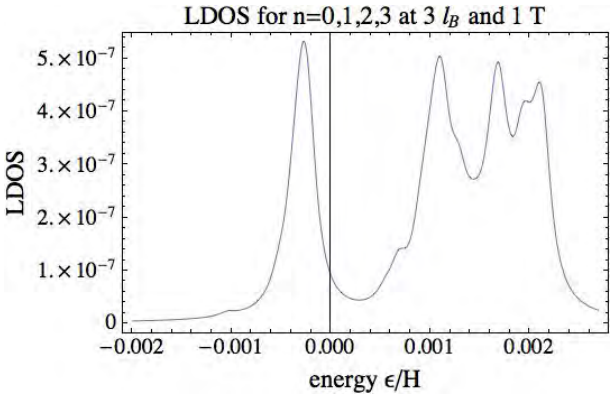

Figure 3.14: A plot of the LDOS at a distance of $3l_B$ from the impurity at 1T, with $n = 0$ - 3 and $m = 0$ - 26.

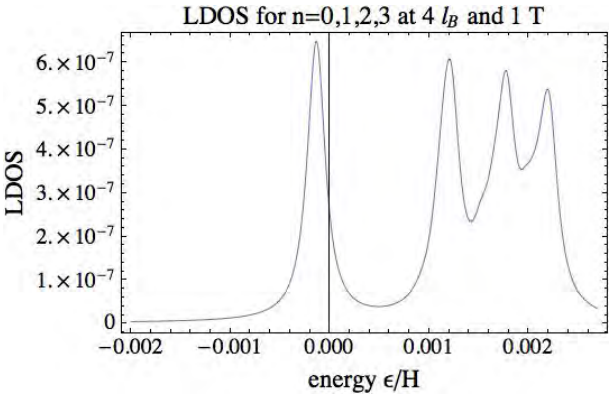

Figure 3.15: A plot of the LDOS at a distance of $4l_B$ from the impurity at 1T, with $n = 0$ - 3 and $m = 0$ - 26.

3.4.2 Case II: B=10 T

The magnetic length in atomic units at B=10 T is $l_B = \sqrt{\hbar/(eB)} \approx 153$ a$_0$. To make a plot for a sample size of 4 $l_B \approx 613$ a$_0$, the cut-off m is found to be 26, as shown in Fig. 3.16.

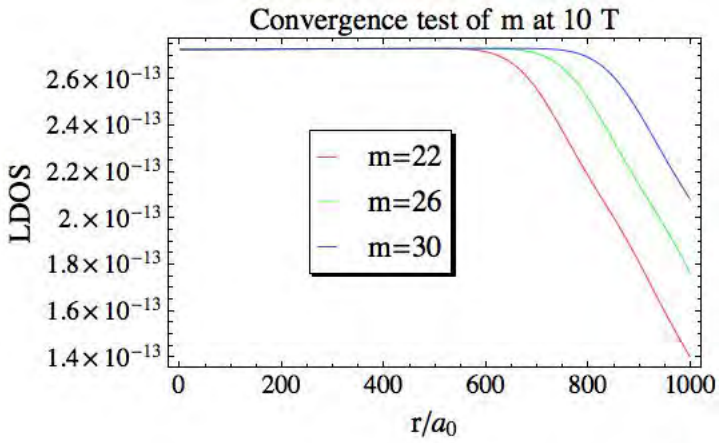

Figure 3.16: A convergence test to determine the appropriate cut-off. For a region of interest of $4l_B \approx 620$, the best cut-off is at $m = 26$ so that it does miss much contribution from large m's and does not include too many m's to adversely affect the computation time.

A density plot of LDOS for up to the third Landau level for a distance up to 4 l_B is shown in Fig. 3.17.

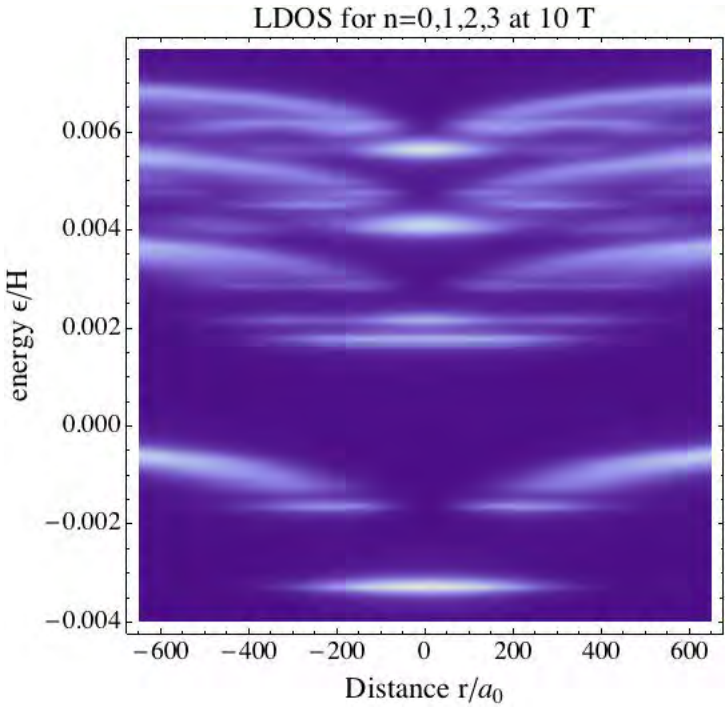

Figure 3.17: A density plot of the LDOS at 10T of the magnetic field, with $n = 0$ - 3 and $m = 0$ - 26.

Plots of LDOS at fixed distances are shown.

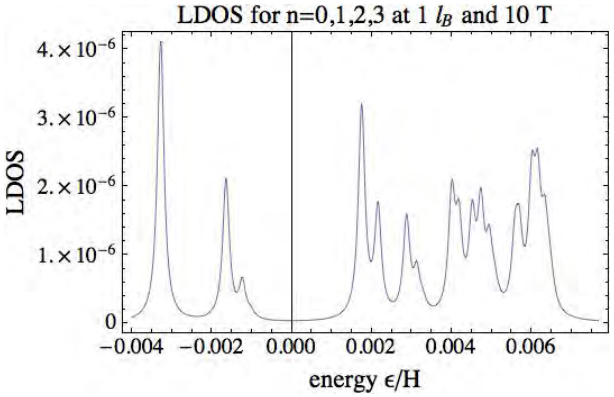

Figure 3.18: A plot of the LDOS at a distance of $1l_B$ from the impurity at 10T, with $n = 0$ - 3 and $m = 0$ - 26.

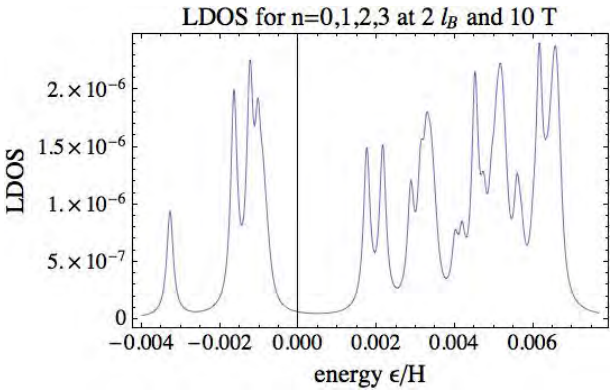

Figure 3.19: A plot of the LDOS at a distance of $2l_B$ from the impurity at 10T, with $n = 0$ - 3 and $m = 0$ - 26.

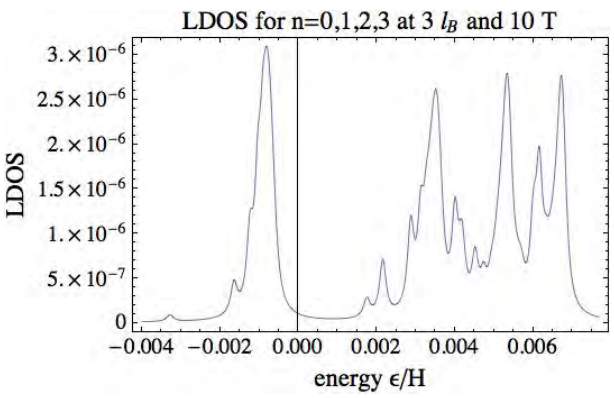

Figure 3.20: A plot of the LDOS at a distance of $3l_B$ from the impurity at 10T, with n = 0 - 3 and m = 0 - 26.

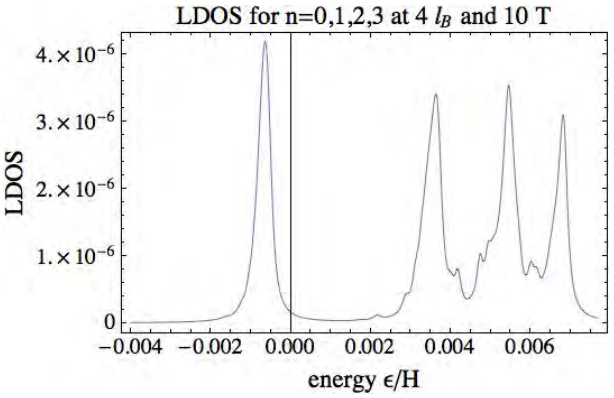

Figure 3.21: A plot of the LDOS at a distance of $4l_B$ from the impurity at 10T, with n = 0 - 3 and m = 0 - 26.

3.5 Comparison with Experimental Result

A recent experimental preprint, posted in November 2013 (later published as [13]), presents an analysis of precisely this problem that we are considering here. In short, it reports the space dependence of the LDOS in the vicinity of a Coulomb impurity in graphene under static magnetic fields. The behavior of the LDOS is studied as a function of magnetic field, and also as a function of the impurity strength, which can be controlled by changing the electronic density, and hence the amount of screening. This preprint appeared simultaneously, and independently, with the calculation described above for the perturbation of the Landau levels and LDOS by the presence of a Coulomb centre. This constituted a fortunate coincidence which allowed an immediate comparison of the predictions summarized in Fig. 3.22 with the corresponding experiment, leading to the validation of the theoretical approach taken here. In addition, it shows the actuality and interest of the topic chosen for this thesis.

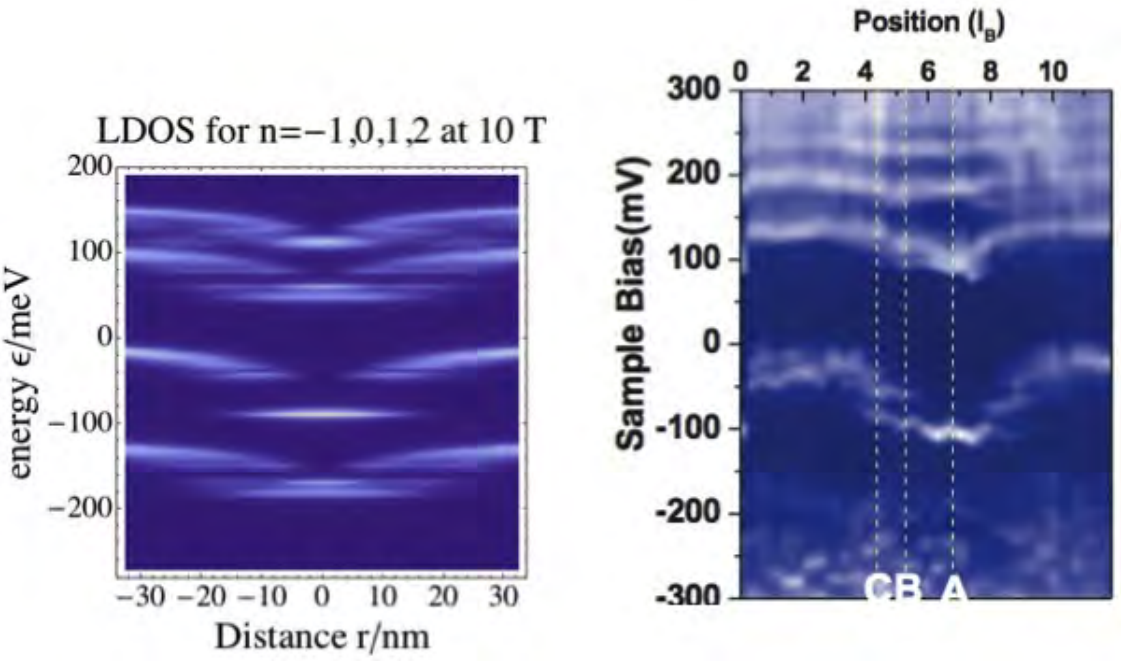

Figure 3.22: Left: the theoretical plot of LDOS for perturbed Landau levels, $n = -1, 0, 1, 2$ at 10 T for a region of up to $4l_B$ ($\approx$ 30 nm). Right: the experimental data of LDOS at 10 T for a similar region of up to about $4l_B$.

In this comparison, several features could be taken note of. The most prominent one is that the extent of bending of Landau levels seems to match between the plots. The downward bending extends for a region of about 2 $l_B \approx 16$ nm for both plots. This is an encouraging confirmation for our perturbation calculation. However, the energy spacing between the 0^{th} and the 1^{st} Landau levels are different in both plots. Since the energy spacing between these two levels is given by

$$\Delta\epsilon_n = \sqrt{2\hbar e v_F^2 B}, \tag{3.65}$$

where the only controlling variable is the magnetic field B. This deviation in energy spacing could indicate that the magnetic field in the experiment may not be at exactly 10 T.

A non-trivial feature in this experimental plot lies in the hole region (n=-1). Unlike the theoretical prediction, the energy spectrum in this region seems to scatter around and does not form a energy band. Since the effective impurity strength calculated in [13] is

about $Z = 1$ which is above the theoretical threshold of $Z_c = 1/2$, this scattered energy spectrum may have an indication of the super-critical resonance. Potentially, this feature could be used as a reference to verify our calculation under a strong magnetic field. Notice that no further investigation was carried on to explain this peculiar feature in [13]. This problem of super-critical collapse under a magnetic field remains elusive and our study could be valuable in addressing this problem.

Chapter 4

Strong Impurity in a Strong B Field

With the extreme case of Landau levels under a perturbative impurity established, one could go on to explore the physics of a strong impurity in a strong B field in graphene.

The Hamiltonian is still given by

$$\hat{H} = v_F \boldsymbol{\sigma} \cdot \left(\hat{\mathbf{p}} + e\hat{\mathbf{A}} \right) + \left(-\frac{g}{r} \right). \tag{4.1}$$

Several methods described in this chapter were employed to attack this problem.

4.1 Power Series Expansion

Using the ansatz

$$\psi_j(r) = \frac{1}{\sqrt{r}} \begin{pmatrix} e^{i(j-1/2)} F(r) \\ i e^{i(j+1/2)} G(r) \end{pmatrix}, \tag{4.2}$$

we have

$$\frac{dF(r)}{dr} - \left(\frac{j}{r} + \frac{eB}{2\hbar} r \right) F(r) + \left(\epsilon + \frac{Z\alpha}{r} \right) G(r) = 0, \tag{4.3}$$

$$\frac{dG(r)}{dr} + \left(\frac{j}{r} + \frac{eB}{2\hbar} r \right) G(r) - \left(\epsilon + \frac{Z\alpha}{r} \right) F(r) = 0, \tag{4.4}$$

where $\epsilon = E/(\hbar v_F)$ and $Z\alpha = g/(\hbar v_F)$. As $F(r)$ and $G(r)$ are coupled, it is sufficient to calculate for one. The second order differential equation for $F(r)$ is

$$\frac{d^2F(r)}{dr^2} + \frac{Z\alpha}{\left(\epsilon + \frac{Z\alpha}{r}\right) r^2}\frac{dF(r)}{dr} - \left[\frac{Z\alpha}{\left(\epsilon + \frac{Z\alpha}{r}\right) r^2}\left(\frac{j}{r} + \frac{eB}{2\hbar}r\right) + \frac{j(j-1) - (Z\alpha)^2}{r^2} - \frac{2\epsilon Z\alpha}{r} + \frac{eB(j+1/2)}{\hbar} - \epsilon^2 + \left(\frac{eB}{2\hbar}\right)^2 r^2\right] = 0. \quad (4.5)$$

In the asymptotic limit of $r \to \infty$, Eq. 4.5 becomes

$$\frac{d^2F(r)}{dr^2} - \left(\frac{eB}{2\hbar}\right)^2 r^2 F(r) = 0, \quad (4.6)$$

whose solution is a parabolic cylinder function which takes the form $\sim \exp\left(-\frac{eB}{4\hbar}r^2\right) f(r)$.

In the asymptotic limit of $r \to 0$, Eq. 4.5 becomes

$$\frac{d^2F(r)}{dr^2} + \frac{1}{r}\frac{dF(r)}{dr} - \left(\frac{j^2 - (Z\alpha)^2}{r^2}\right) F(r) = 0, \quad (4.7)$$

whose solution takes the form r^γ, where $\gamma = \sqrt{j^2 - (Z\alpha)^2}$.

From the behavior of $F(r)$ at large and small distances, we used an ansatz [14]

$$F(r) = r^\gamma \exp\left(-\frac{eB}{4\hbar}r^2\right) \sum_{p=0} a_n r^n, \quad (4.8)$$

$$G(r) = r^\gamma \exp\left(-\frac{eB}{4\hbar}r^2\right) \sum_{p=0} b_n r^n, \quad (4.9)$$

with $a_0 \neq 0$ and $b_0 \neq 0$. Substitution of this ansatz in Eq. 4.3 and 4.4 gives

$$\left(\gamma - j - \frac{eB}{\hbar}r^2\right) \sum_{n=0} a_n r^{\gamma+n-1} + \sum_{n=1} n a_n r^{\gamma+n-1} + (\epsilon r + Z\alpha) \sum_{n=0} b_n r^{\gamma+n-1} = 0, \quad (4.10)$$

$$(\gamma + j) \sum_{n=0} b_n r^{\gamma+n-1} + \sum_{n=1} n b_n r^{\gamma+n-1} - (\epsilon r + Z\alpha) \sum_{n=0} a_n r^{\gamma+n-1} = 0. \quad (4.11)$$

For Eq. 4.10 and Eq. 4.11 to hold, the coefficients of respective r^n must sum to zero.

Explicitly, this means for Eq. 4.10

$$
\begin{aligned}
(\gamma - j)a_0 + Z\alpha b_0 &= 0 \qquad (n = 0), && (4.12)\\
(\gamma - j + 1)a_1 + \epsilon b_0 + Z\alpha b_1 &= 0 \qquad (n = 1), && (4.13)\\
(\gamma - j + n)a_n + \epsilon b_{n-1} + Z\alpha b_n - \frac{eB}{\hbar}\alpha_{n-2} &= 0 \qquad (n \geq 2), && (4.14)
\end{aligned}
$$

and for Eq. 4.11,

$$
\begin{aligned}
(\gamma + j)b_0 - Z\alpha a_0 &= 0 \qquad (n = 0), && (4.15)\\
(\gamma + j + n)b_n + \epsilon a_{n-1} + Z\alpha a_n &= 0 \qquad (n \geq 1). && (4.16)
\end{aligned}
$$

Eliminating b_n for a_n, we then obtain

$$
\begin{aligned}
&(n + \gamma + j - 1)(n^2 + 2n\gamma)a_n + Z\alpha\left[2\epsilon(n + \gamma + j - 1/2)\right]a_{n-1} \\
&\qquad + (n + \gamma + j)\left[\epsilon^2 - \frac{eB}{\hbar}(n + \gamma + j - 1)\right]a_{n-2} = 0. \quad (4.17)
\end{aligned}
$$

Notice that this result is analogous to the one obtained in [14] with the difference that our equation does not contain a mass term. To truncate the Eq. 4.17 at a certain n such that $a_n = a_{n+1} = 0$, we require

$$
\begin{aligned}
K(n, j, \epsilon, B, Z) &= 0 && (4.18)\\
\epsilon^2 &= \frac{eB}{\hbar}(n + \gamma + j), \qquad n = 1, 2, \cdots && (4.19)
\end{aligned}
$$

where $K(n, j, \epsilon, B, Z)$ is a function such that $a_n = K(n, j, \epsilon, B, Z)a_0$. For any integer n, only a certain number of pairs (ϵ, B) satisfy the two conditions. Unlike the conclusion in [14], our solution in principle covers the whole energy range and could provide exact solutions to the problem of Coulomb impurity in a magnetic field if we could obtain such pairs. However, the problem lies that there may be cases that for a certain value of B, ϵ does not exist at all. Our solution does not guarantee the existence of such a pair for every value of B. Hence our solution is incomplete and we should attack the problem with another method.

4.2 Basis Change

A new method is to try a new basis. A natural choice is to use the eigenstates of Landau levels as the basis. The new basis is $(\psi_{n=0,m=0}, \psi_{0,1}, \cdots ; \psi_{1,0}, \psi_{1,0}, \cdots ; \cdots ; \psi_{N,0}, \psi_{N,1}, \cdots)$, with two cut-offs $n \to N$ and $m \to M$. The wave function can then be expressed as

$$\Psi_k(\mathbf{r}) = \sum_n^N \sum_m^M C_{n,m}^k \psi_{n,m}(\mathbf{r}), \tag{4.20}$$

where $\psi_{n,m}(\mathbf{r})$ of Landau levels

$$\psi_{n,m}(\mathbf{r}) = \frac{1}{\sqrt{2}} \begin{pmatrix} \phi_{n-1,m}(\mathbf{r}) \\ \mp i\phi_{n,m}(\mathbf{r}) \end{pmatrix}. \tag{4.21}$$

With the new basis, the goal is to compute the matrix element $H_{nm,n'm'} = \langle \psi_{n,m}(\mathbf{r}) | \hat{H} | \psi_{n',m'}(\mathbf{r}) \rangle$. The advantage of using Landau level eigenstates is that for

$$\begin{aligned} H_{nm,n'm'} &= \langle \psi_{n,m}(\mathbf{r}) | \hat{H} | \psi_{n',m'}(\mathbf{r}) \rangle \\ &= \langle \psi_{n,m}(\mathbf{r}) | \hat{H}^B | \psi_{n',m'}(\mathbf{r}) \rangle + \langle \psi_{n,m}(\mathbf{r}) | \hat{V} | \psi_{n',m'}(\mathbf{r}) \rangle \\ &= H^B_{nm,n'm'} + V_{nm,n'm'}, \end{aligned} \tag{4.22}$$

where $\hat{H}^B = v_F \boldsymbol{\sigma} \cdot \left(\hat{\mathbf{p}} + e\hat{\mathbf{A}} \right)$ and $\hat{V} = -g/r$, the result of the first term has been established

$$H^B_{nm,n'm'} = \sqrt{2\hbar v_F^2 eBn}\,\delta_{n,n'}\delta_{m,m'} = \sqrt{2n}\frac{\hbar v_F}{l_B}\delta_{n,n'}\delta_{m,m'}. \tag{4.23}$$

The second term involves the integration of two Laguerre polynomials [15]

$$V_{nm,n'm'} = \frac{-g(-1)^{m+n'+m'}\sqrt{\pi}}{\sqrt{2l_B^2}} \sqrt{\frac{n!m!}{n'!m'!}} \frac{\Gamma(m-n+1/2)}{\Gamma(n+1)\Gamma(m-n+1)\Gamma(1/2-n')} {}_3F_2\left(\frac{1}{2}, m-n+\frac{1}{2}, -n; m-n+1, \frac{1}{2}-n'; 1\right). \tag{4.24}$$

With Eq. 4.23 and Eq. 4.24, $H_{nm,n'm'}$ can be expressed as an analytical function, which could then greatly speed up the computation progress. After obtaining the matrix ele-

ment, we are able to construct the matrix (Eq. 4.25) and diagonalize it to obtain the coefficient $C^k_{n,m}$ in Eq. 4.20,

$$\begin{pmatrix} H_{00,00} & H_{00,01} & \cdots & H_{00,10} & H_{00,11} & \cdots & \cdots \\ H_{01,00} & H_{01,01} & \cdots & H_{01,10} & H_{01,11} & \cdots & \cdots \\ \vdots & \vdots & \ddots & \vdots & \vdots & \cdots & \cdots \\ H_{10,00} & H_{10,01} & \cdots & H_{10,10} & H_{10,11} & \cdots & \cdots \\ H_{11,00} & H_{11,01} & \cdots & H_{11,10} & H_{11,11} & \cdots & \cdots \\ \vdots & \vdots & \ddots & \vdots & \vdots & \cdots & \cdots \\ \vdots & \vdots & \ddots & \vdots & \vdots & \cdots & \cdots \end{pmatrix} \begin{pmatrix} C_{00} \\ C_{01} \\ \vdots \\ C_{10} \\ C_{11} \\ \vdots \\ \vdots \end{pmatrix} = \epsilon_k \begin{pmatrix} C_{00} \\ C_{01} \\ \vdots \\ C_{10} \\ C_{11} \\ \vdots \\ \vdots \end{pmatrix}. \quad (4.25)$$

Thus the local density of states could then obtained similarly by

$$n(\epsilon, \mathbf{r}) = \sum_k \delta(\epsilon - \epsilon_k) \left|\Psi_k(\mathbf{r})\right|^2 \approx \sum_k \frac{\Gamma^2}{\left(\epsilon - \epsilon_k\right)^2 + \Gamma^2} |\Psi_k(\mathbf{r})|^2. \quad (4.26)$$

To verify this new general matrix, we let $n = n'$ and check whether it reduces to the known results calculated in the previous chapter. Fig. 4.1 to Fig. 4.4 show the encouraging result that this matrix does produce valid results.

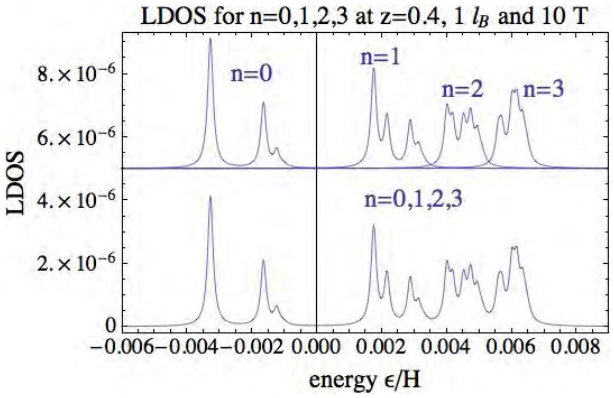

Figure 4.1: Upper panel: the LDOS calculated from the method of using a new basis for each n, $n = 0, 1, 2, 3$. Lower panel: the LDOS calculated from the perturbation calculation. Both panels are computed at a distance of $1l_B$ from the impurity at 10T.

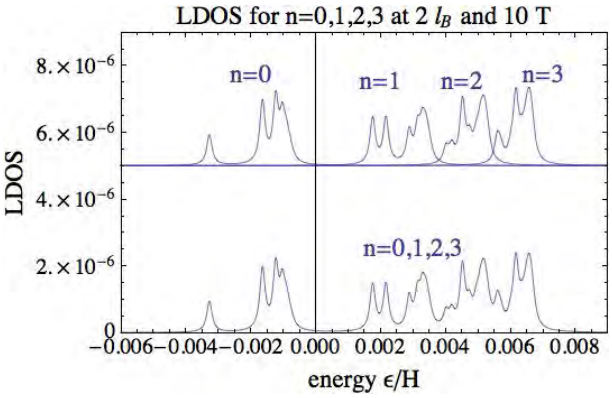

Figure 4.2: Upper panel: the LDOS calculated from the method of using a new basis for each n, $n = 0, 1, 2, 3$. Lower panel: the LDOS calculated from the perturbation calculation. Both panels are computed at a distance of $2l_B$ from the impurity at 10T.

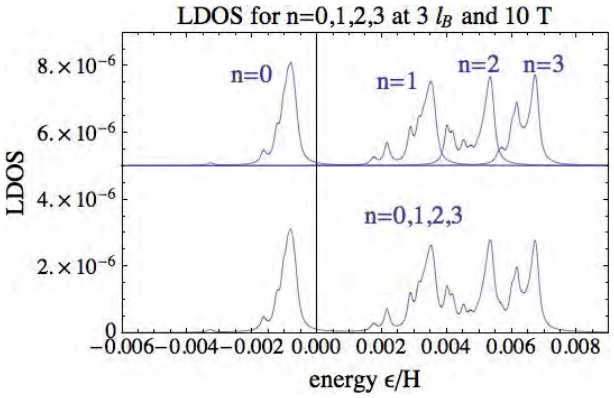

Figure 4.3: Upper panel: the LDOS calculated from the method of using a new basis for each n, $n = 0, 1, 2, 3$. Lower panel: the LDOS calculated from the perturbation calculation. Both panels are computed at a distance of $3l_B$ from the impurity at 10T.

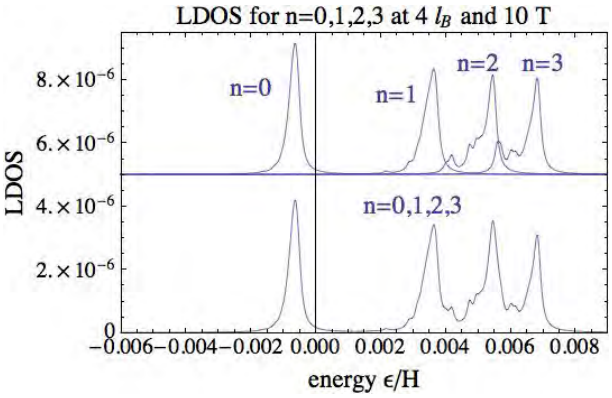

Figure 4.4: Upper panel: the LDOS calculated from the method of using a new basis for each n, $n = 0, 1, 2, 3$. Lower panel: the LDOS calculated from the perturbation calculation. Both panels are computed at a distance of $4l_B$ from the impurity at 10T.

Thus we have validated the local density of states obtained from the new wave function. As the coefficients $C_{n,m}$ are obtained from the matrix in Eq. 4.25 which contains off-diagonal terms, it is good to investigate the effects of these off-diagonal terms. In our basis, these off-diagonal terms correspond to the inter-level couplings.

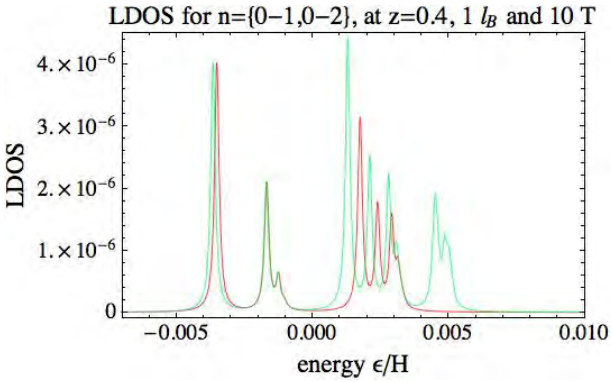

Figure 4.5: A comparison of the LDOS for different ranges of n, $n = 0$ - 1 (red) and $n = 0$ - 2 (green).

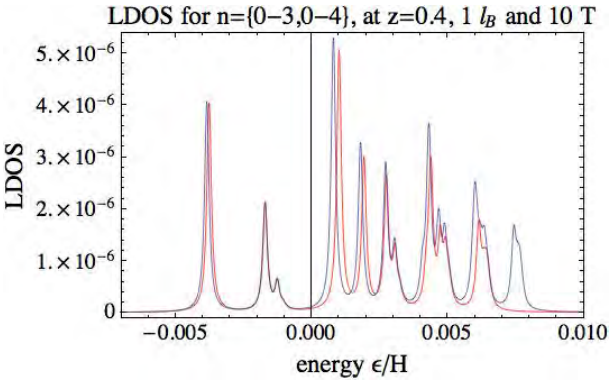

Figure 4.6: A comparison of the LDOS for different ranges of n, $n = 0$ - 3 (red) and $n = 0$ - 4 (blue).

The trend is that when we include more Landau levels (n increases), the peaks are pushed to the lower energy and the peak heights increase.

Next we would like to study the effect of impurity strength on the local density of states.

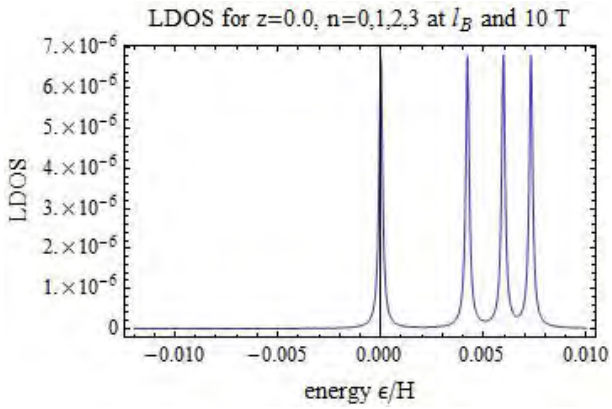

Figure 4.7: The LDOS for $n = 0$ - 3 at 10 T and an impurity strength of g=0.00.

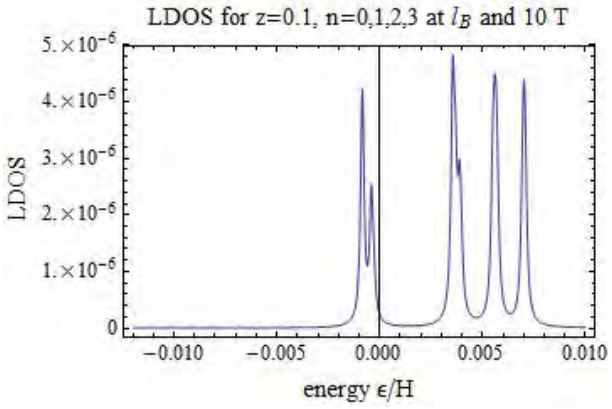

Figure 4.8: The LDOS for $n = 0$ - 3 at 10 T and an impurity strength of g=0.10.

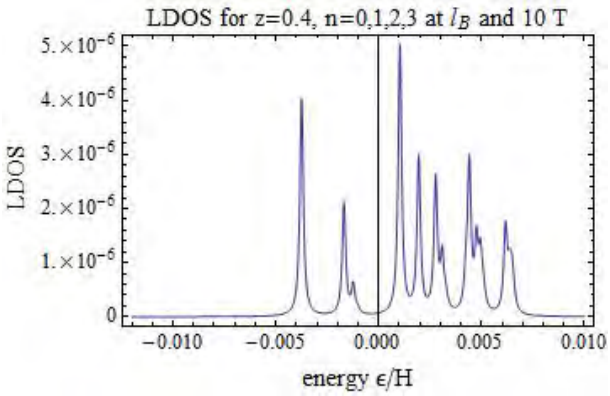

Figure 4.9: The LDOS for $n = 0$ - 3 at 10 T and an impurity strength of g=0.40.

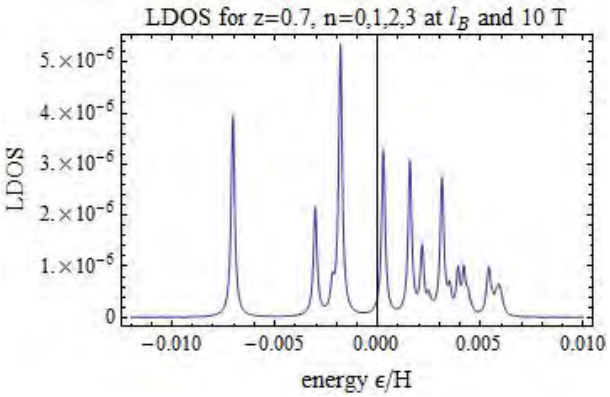

Figure 4.10: The LDOS for $n = 0$ - 3 at 10 T and an impurity strength of g=0.70.

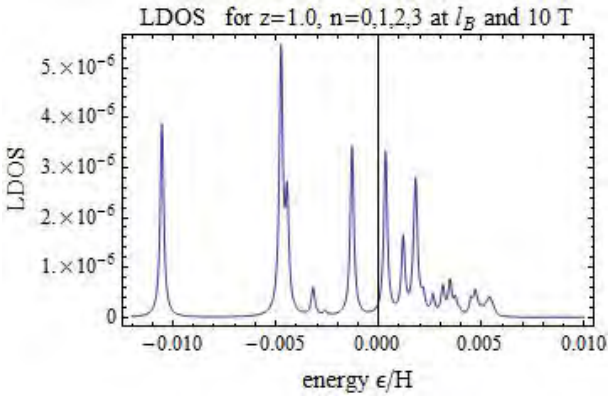

Figure 4.11: The LDOS for $n = 0$ - 3 at 10 T and an impurity strength of g=1.00.

The impurity lifts the degeneracy of Landau levels as shown by the peak splitting. The peak positions are also in general pushed to the lower energy region.

Notice that near the origin where the effect of the magnetic field tends to zero, the behavior of the probability function should approach the Coulomb result with a fast oscillation shown in Fig. 2.4. However, this expected fast oscillation governed by r^γ term from Eq. 4.8 does not appear. We speculate that this is due to the difference in the characteristic length scale. The fast oscillation characterizing the super-critical region has a length scale of Bohr radius a_0 while the length scale for $\Psi_k(\mathbf{r})$ is in terms of the magnetic length l_B. Since $l_B \gg a_0$, the feature near the origin broaden out and the wave

function $\Psi_k(\mathbf{r})$ may not capture the fine details close to the origin.

4.3 Change of Basis with Modification

Previous methods suffer limitations from different aspects. A natural idea is to combine the two methods in a search of a new ansatz. The essential principle for this new ansatz is that it should be able to capture the electronic behavior near the origin and it should be easy to select a cut-off from the series. Thus the new ansatz is proposed as

$$\tilde{\Psi}_k(\mathbf{r}) = r^\gamma \Psi_k(\mathbf{r}) = r^\gamma \sum_{n,m} C^k_{n,m} \psi_{n,m}(\mathbf{r}), \tag{4.27}$$

where $\gamma = \sqrt{j^2 - (Z\alpha)^2}$ and $\psi_{n,m}(\mathbf{r})$ is the Landau level eigenstates. In this ansatz, the shot-distance behavior is accounted for by the term r^γ and the cut-off is settled by choosing the Landau level eigenstates.

Following similar procedures, we know that

$$\langle \tilde{\Psi}_{k'}(\mathbf{r}) | \hat{H} | \tilde{\Psi}_k(\mathbf{r}) \rangle = E_k \langle \tilde{\Psi}_{k'}(\mathbf{r}) | \tilde{\Psi}_k(\mathbf{r}) \rangle = E_k S, \tag{4.28}$$

where S is the overlap function. Thus the eigen-energies are computed by solving the generalized eigenvalue condition

$$\det \left(E_k - S^{-1} \langle \tilde{\Psi}_{k'}(\mathbf{r}) | \hat{H} | \tilde{\Psi}_k(\mathbf{r}) \rangle \right) = 0, \tag{4.29}$$

where S^{-1} is the inverse of S. A matrix analogous to Eq. 4.25 is contructed and then diagonalized to obtain the coefficient $C^k_{n,m}$.

To check the validity of the solution from the new ansatz,, we compare it with established energy spectra from Landau levels and perturbation calculation.

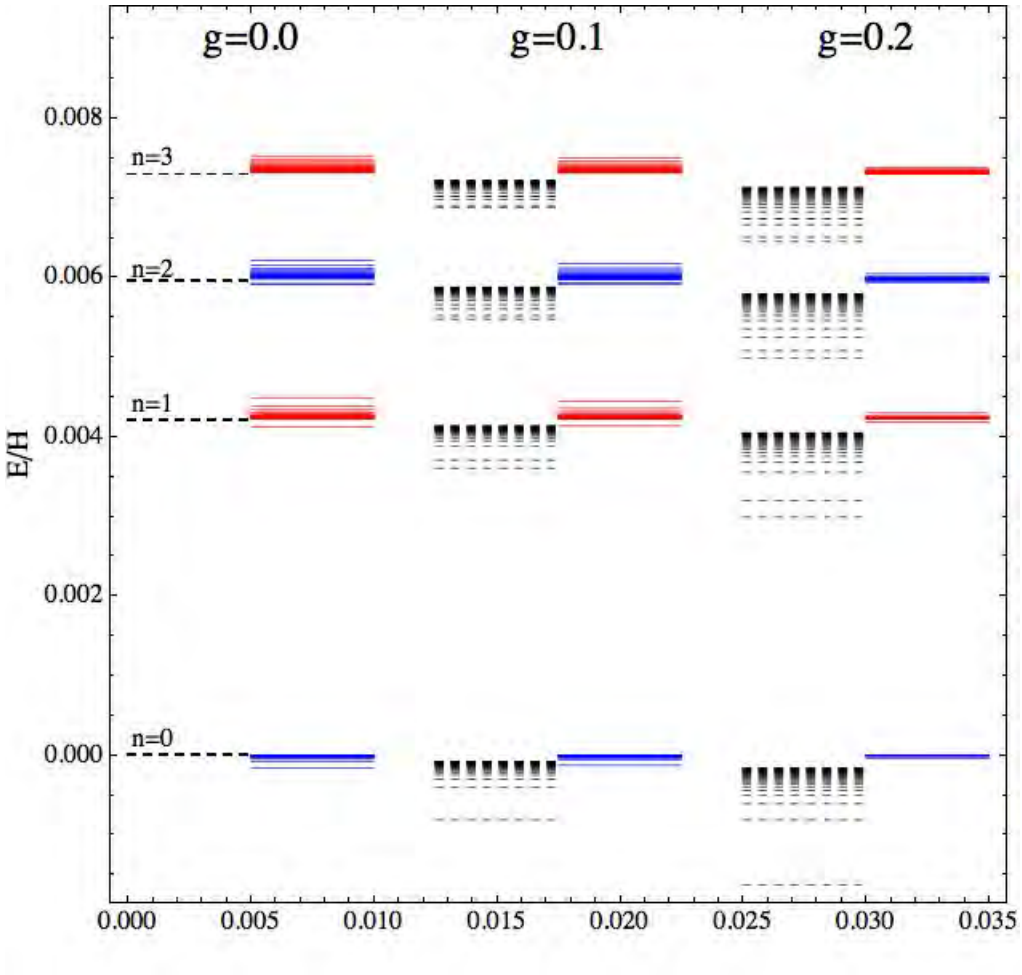

Figure 4.12: A comparison of the energy spectra from the perturbation calculation (dashed) with that of the new ansatz (solid) at different impurity strengths.

Notice that the the energy spectra from this new ansatz is in the correct region of the Landau levels. However, as the impurity strength increases, the new energy spectra do not represent the splitting very well. A possible explanation is that this brute-force introduction of the new ansatz is in a way equivalent to the introduction of an uncontrolled perturbation. In this basis, the new wave functions are not orthogonal to each other. The overlap between two functions is rather large and this may introduce errors in the computation.

Chapter 5

Future Direction

5.1 Semi-classical Approach

Currently, all three methods are not working out well in extracting an analytical solution of the electronic response around a Coulomb impurity in a strong magnetic field. Thus we want to go back to a semi-classical approach in an attempt to learn any useful information to treat this problem of super-critical collapse in a strong magnetic field.

For a case without a magnetic field, the semi-classical Hamiltonian [3] ($\hbar = 1$) is

$$H = v_f \left(|\mathbf{p}| - \frac{g}{r} \right), \tag{5.1}$$

where $g = Ze^2/(4\pi\epsilon_0 v_F)$. Since $|\mathbf{p}| = \sqrt{p_r^2 + l^2/r^2}$, the energy is

$$E = v_F \left(\sqrt{p_r^2 + \frac{l^2}{r^2}} - \frac{g}{r} \right), \tag{5.2}$$

or

$$p_r^2 = \left(\epsilon^+ \frac{g}{r} \right)^2 - \frac{l^2}{r^2}, \tag{5.3}$$

where $\epsilon = E/v_F$.

Depending on the values of ϵ, g and l, p_r^2 varies in different ways. Fig. 5.1 to Fig. 5.4 show the different cases.

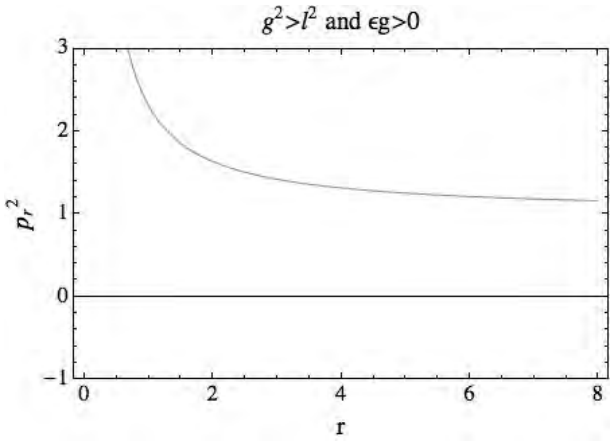

Figure 5.1: Graph of the radial momentum against the distance to the impurity.

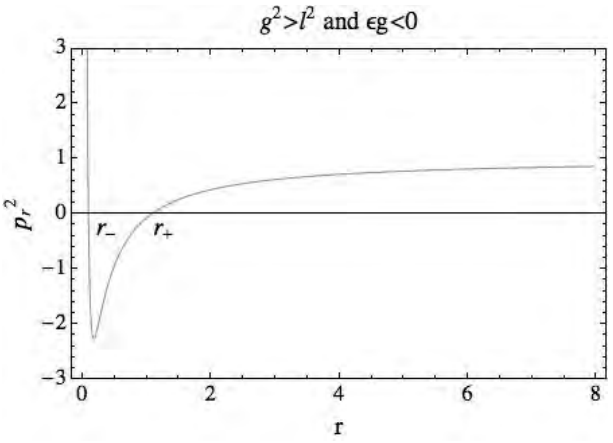

Figure 5.2: Graph of the radial momentum against the distance to the impurity.

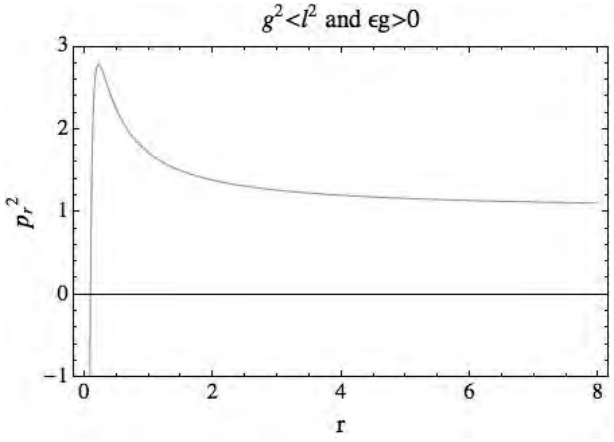

Figure 5.3: Graph of the radial momentum against the distance to the impurity.

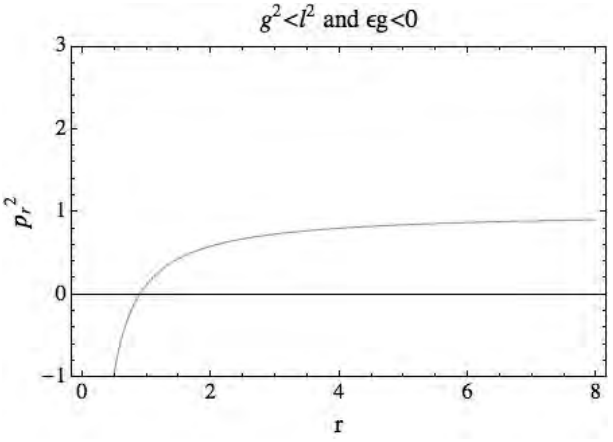

Figure 5.4: Graph of the radial momentum against the distance to the impurity.

Considering the case of an electron in the super-critical region, which corresponds to the situation in Fig. 5.2, the roots of Eq. 5.3 are

$$r_- = \frac{l-g}{\epsilon}, \qquad r_+ = -\frac{l+g}{r}. \tag{5.4}$$

Fig. 5.2 implies that there is a cylindrical barrier of a width $d = r_+ - r_-$ which separates the collapse trajectory and the scattering trajectory. Thus electrons within the distance of r_- reside on the resonant states which could be obtained by applying the Bohr-Sommerfeld

quantization rule,

$$\oint \mathbf{p} \cdot d\mathbf{r} = nh. \tag{5.5}$$

The corresponding radial quantization rule is thus

$$\int_{r_0}^{r_-} p_r dr = n\pi\hbar, \tag{5.6}$$

$$\int_{r_0}^{r_-} \sqrt{\left(\epsilon^+ \frac{g}{r}\right)^2 - \frac{l^2}{r^2}} dr = n\pi\hbar, \tag{5.7}$$

where the lower bound r_0 is introduced to respect the fact that the impurity atom has a finite size. Notice from Fig. 5.2 that the leading contribution of the integration is from the vicinity of the impurity. It is reasonable to simplify Eq. 5.7

$$\int_{r_0}^{r_-} \frac{\sqrt{g^2 - l^2}}{r} dr = \int_{r_0}^{r_-} \frac{\gamma}{r} dr = n\pi\hbar. \tag{5.8}$$

The solution of this integration is

$$\gamma \ln\left(\frac{g}{r_0 \epsilon}\right) = n\pi\hbar, \tag{5.9}$$

or

$$\epsilon_n = \frac{g}{r_0} \exp\left(-\frac{n\pi\hbar}{\gamma}\right). \tag{5.10}$$

For the case in a magnetic field, a similar procedure could be applied. The respective equation for the radial equation [6] is

$$p_r^2 = \left(\frac{\epsilon}{l_B} + \frac{g}{r}\right)^2 - \left(\frac{j}{r} - \frac{r}{2l_B^2}\right)^2, \tag{5.11}$$

where $\epsilon = (El_B)/(\hbar v_F)$.

Fig. 5.5 to Fig. 5.8 show the possible dependence of the radial momentum on the distance to the impurity.

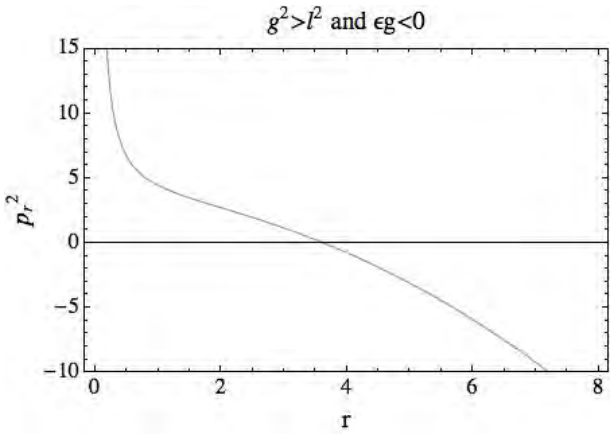

Figure 5.5: Graph of the radial momentum against the distance to the impurity for $j = 1/2$, g=0.6 under a magnetic field such that $l_B = 1$ for negative ϵ.

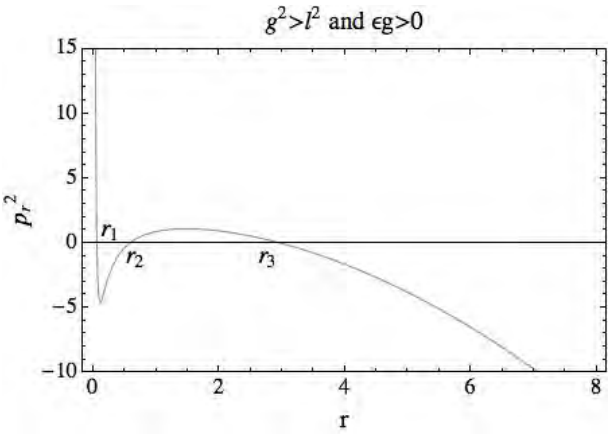

Figure 5.6: Graph of the radial momentum against the distance to the impurity for $j = 1/2$, g=0.6 under a magnetic field such that $l_B = 1$ for positive ϵ.

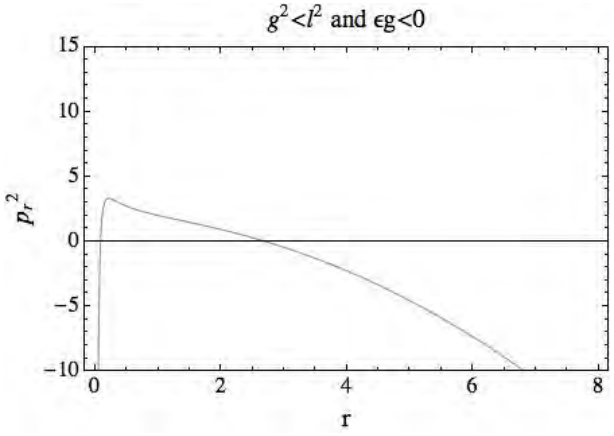

Figure 5.7: Graph of the radial momentum against the distance to the impurity for $j = 1/2$, g=0.4 under a magnetic field such that $l_B = 1$ for negative ϵ.

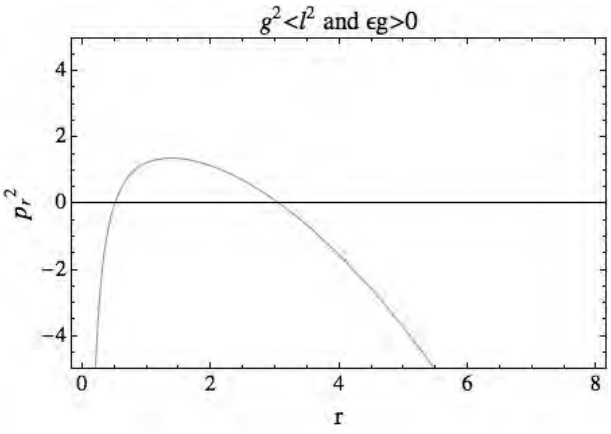

Figure 5.8: Graph of the radial momentum against the distance to the impurity for $j = 1/2$, g=0.4 under a magnetic field such that $l_B = 1$ for positive ϵ.

Similarly, the zeros of Eq. 5.11 are shown in Fig. 5.6

$$r_1 = l_B\epsilon - \sqrt{-2gl_B^2 + 2jl_B^2 + l_B^2\epsilon^2}, \tag{5.12}$$

$$r_2 = -l_B\epsilon + \sqrt{2gl_B^2 + 2jl_B^2 + l_B^2\epsilon^2}, \tag{5.13}$$

$$r_3 = l_B\epsilon + \sqrt{-2gl_B^2 + 2jl_B^2 + l_B^2\epsilon^2}. \tag{5.14}$$

However due to time constraint, the work currently stops at extracting the leading contribution to the integration and finding the semi-classical energy. It is problematic in accounting of the imaginary p_r in the region between r_1 and r_2.

Alternatively, we can approach the problem from the potential. By following the effective potential by [6],

$$U_{eff} = \frac{j^2 - g^2}{r^2} + \frac{2\epsilon g}{r} + \frac{r^2}{4}, \tag{5.15}$$

we note that the problem is essentially a problem of double potential wells (Fig. 5.9).

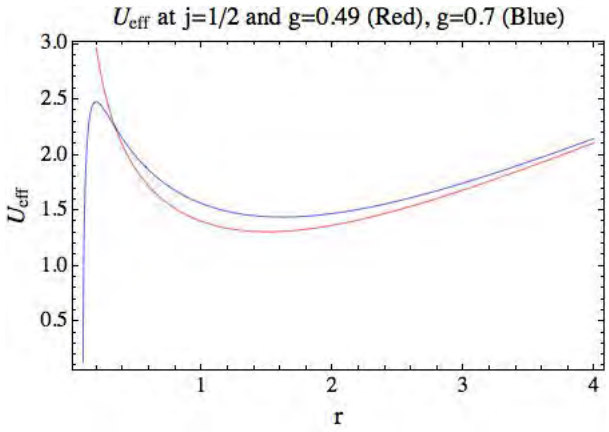

Figure 5.9: The effective potential for an angular momentum channel $j = 1/2$ for the sub-critical region ($g = 0.49$ (Red)) and for the super-critical region ($g = 0.7$ (Blue)). The threshold value of g is $g_c = 1/2$.

Due to the cut-off radius near the impurity, the Coulomb potential is regularized, forming a deep narrow well. The magnetic field essentially confine the electrons from escaping to the infinity, resulting in the relatively shallow and broad well. The strength of the Coulomb impurity and the magnetic field control the overall shape of the effective potential. When the Coulomb impurity is below the threshold, the finite potential barrier (Fig. 5.9) between the two wells disappears. But when the Coulomb impurity is well above the threshold, the potential barrier could be so high that electrons within the inner well are confined inside and forming the resonant states. A line of approach is to compute the energy levels in both wells separately and then coupled the two sets of energy levels together, with the coupling strength determined by the barrier. Another method is to solve the exact Schrödinger equation by matching the boundary conditions. In such a

way, it may be possible to extract a solution for energy spectrum of the super-critical region under a strong magnetic field.

5.2 Numerical Study

If the methods mentioned above do not provide enough insights of the problem of super-critical collapse in a strong field, we can still employ a numerical study to obtain an approximate solution. We consider a generic Hamiltonian of graphene

$$\hat{H} = \hbar v_F \left(\frac{1}{\hbar} \boldsymbol{\sigma} \cdot \left(\hat{\mathbf{p}} + e\hat{\mathbf{A}} \right) + V(r) \right), \tag{5.16}$$

and the wave function is

$$\psi_l(\mathbf{r}) = \frac{1}{\sqrt{r}} \begin{pmatrix} F(r) \exp^{i(l-1)\theta} \\ iG(r) \exp^{il\theta} \end{pmatrix}. \tag{5.17}$$

Solving the eigenvalue problem $\hat{H}\psi_l = E\psi_l$ gives

$$\begin{pmatrix} V(r) - \epsilon & \frac{\partial}{\partial r} + \frac{l-1/2}{r} - \frac{r}{2l_B^2} \\ -\frac{\partial}{\partial r} + \frac{l-1/2}{r} - \frac{r}{2l_B^2} & V(r) - \epsilon \end{pmatrix} \begin{pmatrix} F(r) \\ G(r) \end{pmatrix} = 0, \tag{5.18}$$

where $\epsilon = E/(\hbar v_F)$. To further simplify the expression, we let

$$\begin{pmatrix} F(r) \\ G(r) \end{pmatrix} = (\epsilon - V(r))^{1/2} \begin{pmatrix} \alpha(r) \\ \beta(r) \end{pmatrix}, \tag{5.19}$$

and Eq. 5.18 becomes

$$\begin{pmatrix} V(r) - \epsilon & \frac{\partial}{\partial r} - \frac{1}{2(\epsilon - V(r))} \frac{\partial V}{\partial r} + \frac{l-1/2}{r} - \frac{r}{2l_B^2} \\ -\frac{\partial}{\partial r} + \frac{1}{2(\epsilon - V(r))} \frac{\partial V}{\partial r} + \frac{l-1/2}{r} - \frac{r}{2l_B^2} & V(r) - \epsilon \end{pmatrix} \begin{pmatrix} F(r) \\ G(r) \end{pmatrix} = 0. \tag{5.20}$$

It is straightforward to decouple α and β in Eq. 5.20 and we have

$$\frac{\partial^2\alpha}{\partial r^2} + (\bar{\epsilon} - \mathrm{U1}(r))\,\alpha = 0, \tag{5.21}$$

$$\frac{\partial^2\beta}{\partial r^2} + (\bar{\epsilon} - \mathrm{U2}(r))\,\beta = 0, \tag{5.22}$$

where $\bar{\epsilon} = \epsilon^2$ and

$$\begin{aligned}\mathrm{U1} = &-\frac{j+1/2}{l_B^2} + \frac{j^2-j}{r^2} + \frac{r^2}{4l_B^4} - V^2 + 2\epsilon V \\ &- \frac{r}{2l_B^2(\epsilon - V)}\frac{\partial V}{\partial r} + \frac{j}{r(\epsilon - V)}\frac{\partial V}{\partial r} + \frac{3}{4(\epsilon - V)^2}\left(\frac{\partial V}{\partial r}\right)^2 + \frac{1}{2(\epsilon - V)}\frac{\partial^2 V}{\partial r^2},\end{aligned} \tag{5.23}$$

$$\begin{aligned}\mathrm{U2} = &-\frac{j-1/2}{l_B^2} + \frac{j^2+j}{r^2} + \frac{r^2}{4l_B^4} - V^2 + 2\epsilon V \\ &+ \frac{r}{2l_B^2(\epsilon - V)}\frac{\partial V}{\partial r} - \frac{j}{r(\epsilon - V)}\frac{\partial V}{\partial r} + \frac{3}{4(\epsilon - V)^2}\left(\frac{\partial V}{\partial r}\right)^2 + \frac{1}{2(\epsilon - V)}\frac{\partial^2 V}{\partial r^2},\end{aligned} \tag{5.24}$$

are the respective effective potentials with $j = l - 1/2$. We observe that Eq. 5.21 and Eq. 5.22 take the form of a usual Schrödinger equation. Thus the energy spectrum for different angular momentum channels could be obtained similarly once the scalar potential $V(r)$ is known.

In the numerical study, we can employ the regularized Coulomb potential in the form of

$$V(r) = -\frac{g}{\sqrt{r^2 + a^2}}. \tag{5.25}$$

The effective potentials U1 and U2 are shown in Fig. 5.10 and Fig. 5.11

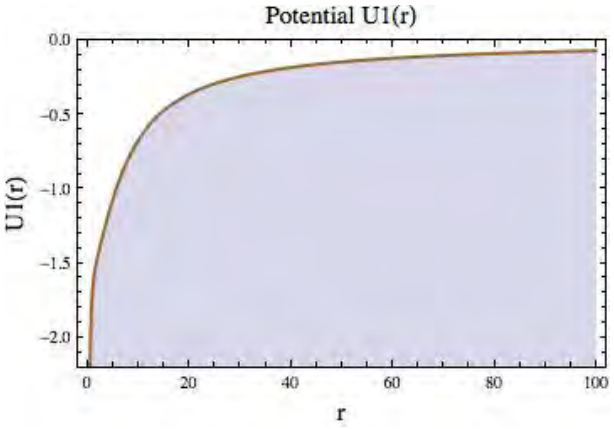

Figure 5.10: Effective potential U1(r) at $\epsilon = 10$ and $g = 0.4$ for the angular momentum channel of $j = 1/2$.

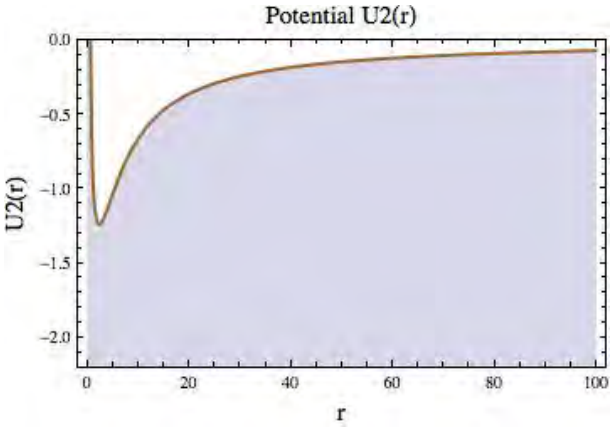

Figure 5.11: Effective potential U2(r) at $\epsilon = 10$ and $g = 0.4$ for the angular momentum channel of $j = 1/2$.

It should be relatively easy to solve Eq. 5.21 and Eq. 5.22 for the energy spectrum numerically. However, we should be careful in evaluating these solutions as some of them are not corresponding to bound states. A numerical study of the energy spectrum at different angular momentum channels was obtained in [6] for the sub-critical region. This could be used as a reference to check our solution. However, the energy spectrum for the super-critical region was not investigated in [6] and our study could remain useful.

Chapter 6

Conclusion

This thesis has reviewed the properties of graphene and the occurrence of super-critical atomic collapse. It has also shown the result of a weak Coulomb impurity in a magnetic field to establish the limiting case. In this case, our calculation approach was validated almost in real time with the appearance of the experimental paper [13]. The bending of the Landau levels in the vicinity of the charged impurity observed in those experiments is entirely captured by our perturbative treatment and our prediction for the dependence of the LDOS on energy and distance to the impurity. Various methods have been employed to attack the problems and no satisfactory solutions are obtained so far. A potential semi-classical approach could provide a hint on addressing this problem of super-critical collapse in a magnetic field. Lastly, a numerical study could be carried out to provide some insights of the problem.

The experimental observation of supercritical collapse in graphene in 2013 has been a major milestone with regards to a prediction that is decades-old and has a long story in quantum electrodynamics under strong fields. The versatility of graphene as a condensed matter system, especially the fact that it is planar, can easily host virtually any adsorbed species, and allows direct probing of its electronic excitations via STM, ARPES, and other probes, certainly means that the problem of supercritical collapse will be further pursued under various conditions, with the ultimate goal of achieving a system that can be driven in and out of the supercritical regime on demand. An external magnetic field can potentially be such a tool. But a magnetic field brings also many new features to the problem. One of them is the much higher complexity of the theoretical problem since the Dirac equation is not exactly solvable anymore in the presence of the field. This is a major

technical complication, and similar to the absence of exact solutions for the hydrogen atom under an arbitrarily strong magnetic field. Since the topic is of current theoretical and experimental interest, the immediate goal is to dedicate effort to a numerical solution of this problem that is valid at all fields, in order to be able to unveil the properties of the supercritical regime. This will be done beyond, and despite the conclusion of this final year project, hoping that, capitalizing on this last effort, a publication can emerge addressing that regime, and eventually explaining some features of the experiments reported in [13] that remain unaccounted for.

Acknowledgments

I would like to express my deep and heartfelt thanks to my supervisor, Prof. Vitor Manuel Pereira. I would also like to thank all who have helped me in one way or another. Finally, I would like to thank the reader who has persevered this far.

References

[1] Novoselov, K. S. *et al.* Electric field effect in atomically thin carbon films. *Science* **306**, 666–669 (2004).

[2] Pereira, V. M., Nilsson, J. & Castro Neto, A. H. Coulomb impurity problem in graphene. *Phys. Rev. Lett.* **99**, 166802 (2007).

[3] Shytov, A. V., Katsnelson, M. I. & Levitov, L. S. Vacuum polarization and screening of supercritical impurities in graphene. *Phys. Rev. Lett.* **99**, 236801 (2007).

[4] Wang, Y. *et al.* Observing atomic collapse resonances in artificial nuclei on graphene. *Science* **340**, 734–737 (2013).

[5] Gamayun, O. V., Gorbar, E. V. & Gusynin, V. P. Magnetic field driven instability of a charged center in graphene. *Phys. Rev. B* **83**, 235104 (2011).

[6] Zhang, Y., Barlas, Y. & Yang, K. Coulomb impurity under magnetic field in graphene: A semiclassical approach. *Phys. Rev. B* **85**, 165423 (2012).

[7] Wallace, P. R. The band theory of graphite. *Phys. Rev.* **71**, 622–634 (1947).

[8] Castro Neto, A. H., Guinea, F., Peres, N. M. R., Novoselov, K. S. & Geim, A. K. The electronic properties of graphene. *Rev. Mod. Phys.* **81**, 109–162 (2009).

[9] Semenoff, G. W. Condensed-matter simulation of a three-dimensional anomaly. *Phys. Rev. Lett.* **53**, 2449–2452 (1984).

[10] Novikov, D. S. Elastic scattering theory and transport in graphene. *Phys. Rev. B* **76**, 245435 (2007).

[11] Landau, L. D. & Lifshitz, L. M. *Quantum Mechanics: Non-Relativistic Theory* (Pergamon Press, New York, 1981).

[12] Goerbig, M. O. Quantum hall effects. *arXiv* 0909–1998 (2009).

[13] Luican-Mayer, A. *et al.* Screening charged impurities and lifting the orbital degeneracy in graphene by populating landau levels. *Phys. Rev. Lett.* **112**, 036804 (2014).

[14] Ho, C.-L. & Khalilov, V. R. Planar dirac electron in coulomb and magnetic fields. *Phys. Rev. A* **61**, 032104 (2000).

[15] Mavromatis, H. A. & Alassar, R. S. Two new associated laguerre integral results. *Appl. Math. Lett.* **14**, 903–905 (2001).